UiT The Arctic University of Norway

Faculty of Science and Technology

Department of Physics and Technology

Numerical and experimental investigation of absorbing polymer films suitable for boundary photoacoustic imaging

Marte Salmi

FYS-3941 Master's thesis in applied physics and mathematics / 30 ECTS / July 2020

Abstract

One of the main challenges in conventional photoacoustic methods, is that thin biological samples typically have low optical absorption in the visible region. Therefore, it is often necessary to stain or label the sample with a color which provide sufficient absorption for the laser wavelength used in the scanning system. Unfortunately, the labeling often introduce unwanted properties to the biological sample of interest. Such properties are often difficult to separate from the actual properties of the object itself. Therefore, it is a rapidly growing interest in the field of biological imaging to develop a label-free imaging method. In this thesis, such a method is proposed by creating a photoacoustic film consisting of a solution of polydimethylsiloxane and black toner particles gathered from a laser printer cartridge. The film is then placed in the vicinity of the object to be imaged, and then reconstruct acoustic properties inside the object. The proposed method is denoted as a boundary photoacoustic method, since the image reconstruction depends fully on external wave sources. To benchmark and model the system, two non-biological photoacoustic films are fabricated with different amounts of toner particles. The first one has 0.5 grams of toner particles, while the other one has 1 gram of toner particles. The maximum of the mean intensity of the acoustic signal obtained from a small area of the PAF, increased by 9 % when the amount of toner particles was doubled.

1

Acknowledgments

First and foremost, I would like to thank Frank for giving me the idea for this thesis. You have been an invaluable source for guidance and knowledge. Further, I want to express my gratitude to Krishna. Your contribution through discussions and suggestions have been highly appreciated. It has been a pleasure to work with both of you, and I could not have done it without your help.

I also want to thank Habib for all your help in conducting the experimental part of this thesis, and sharing your know-how with me. It has been very educational.

Lastly, to Martin and Hela: thank you for keeping my spirits up when times got tough.

Marte Salmi

Tromsø, July 2020

Contents

List of Figures

List of Tables

Abbreviations

AR-PAM	Acoustic-Resolution PhotoAcoustic Microscopy
BPAM	Boundary PhotoAcoustic Method
DBC	Dirichlet Boundary Condition
FWHM	Full Width at Half Maximum
NIR	Near InfraRed
OR-PAM	Optical-Resolution PhotoAcoustic Microscopy
PACT	PhotoAcoustic Computed Tomography
PAF	PhotoAcoustic Film
PAI	PhotoAcoustic Imaging
PAM	PhotoAcoustic Microscopy
PDE	Partial Differential Equation
PDMS	PolyDiMethylSiloxane
PVDF	PolyVinyliDene Fluoride
RPM	Revolutions Per Minute
US	UltraSound
UT	Ultrasonic Transducer
UV	UltraViolet

Chapter 1

Introduction

The main purpose of this master project has been to investigate polymer films suitable for generating ultrasonic waves from laser excitation. The films in this thesis consisted of a coating produced from mixing nano-particles and a polymer-base. The motivation for developing such a film which we will refer to as a photoacoustic film (PAF), is to create new label-free methods for photoacoustic imaging. This can be done by placing a PAF in the vicinity of the object to be imaged, and then reconstruct acoustical properties inside the object (e.g. phase velocity or attenuation) using an inversion method. We will denote the proposed method as a boundary photoacoustic method (BPAM), since the image reconstruction totally depends on external wave sources, or sources at the boundary of the object to be imaged. The BPAM approach is so far quite unexplored in the literature, while conventional photoacoustic imaging (PAI) and photoacoustic microscopy (PAM) which both depend on laser absorption inside the object, have achieved a rapidly growing interest.

The main challenge with conventional photoacoustic methods, is that thin biological samples typically have rather low optical absorption coefficients in the visible region. Due to this, it is often necessary to stain or label the sample with a color that provide sufficient absorption for the used laser wavelength. Such a labeling is known to introduce unwanted properties to the object under investigation, which often is difficult to separate from its "unlabeled" properties. It is therefore in biological imaging now a rapidly growing interest for developing label-free imaging methods.

Most of the impact in this thesis has been put on the following subjects:

Numerical investigation of PAFs with the purpose to explore physical parameters like film thickness, absorption coefficient and laser beam width in COMSOL Multiphysics.

Experimental investigation of PAFs to determine the increase in intensity of the acoustic signal generated by the PAF, for different ratios of nano-particles to base. A high light absorption, and thus large intensity acoustic waves, are the main goal when fabricating PAFs.

Comparison of experimental and numerical data to determine if the model in COMSOL Multiphysics was accurate enough to function as an estimate for real-life observations.

1.1 Photoacoustic Imaging

For regular ultrasound imaging, high-frequency sound waves are emitted from an ultrasonic transducer (UT) to a patient. Here, they are reflected or scattered from the different tissues inside the patients body [1]. Echoed signals are then received by the same transducer, and converted into an image. A major drawback of this technique is speckle occurring in the images, due to scattering [2; 3].

Photoacoustic imaging (PAI) overcomes this obstacle with ease, by employing a hybrid technique consisting of a laser and an ultrasonic transducer. Laser light is delivered to the tissue of interest, which absorbs it. The absorbed energy causes optical induced ultrasound waves to be emitted from the tissue [2]. The sound waves are then received by an UT, and used to reconstruct an image. Photoacoustic imaging takes advantage of the absorption of light in tissues, rather than acoustic scattering as in regular ultrasound [3]. Consequently, speckle does not occur in photoacoustic imaging [2].

The wavelength of the laser light is chosen depending on the samples to be imaged. For imaging of thick biological samples and small animals [4], such as mice, wavelengths in the near infrared (NIR) spectrum is used to obtain deeper penetration of light into the tissue [2]. The NIR region is defined between 800 nm to 2500 nm [5]. For thinner biological samples, ultra-violet (UV) or visible light may be utilized. For reference, the electromagnetic spectrum is included in figure 1.1. The duration of the laser pulse is short, < 10 ns [2]. When laser light is absorbed in tissue, it causes a local increase in temperature, which in turn leads to a small increase in pressure through thermoelastic expansion. When the pressure relaxes back to its initial value, ultrasound waves are released and start to propagate through the tissue [3]. Since the light waves from the laser only have to travel one-way, it is possible to achieve deeper tissue penetration compared to other optical imaging methods [2]. In addition, the scattering of ultrasound waves is weaker than scattering of light waves in tissue [2], ensuring high spatial resolution in the images.
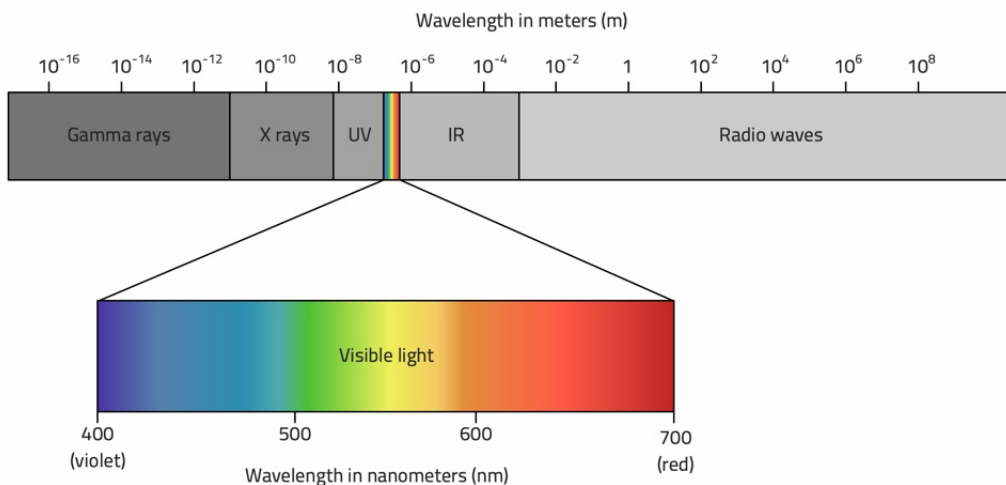
Figure 1.1: The electromagnetic spectrum. In PAI, wavelengths in the regions of near-infrared, UV and visible light are used. The near-infrared region is defined between wavelengths of 800 nm to 2500 nm [5]. Image from [6]

Furthermore, different components of tissue may be targeted by irradiating the tissue with the dominant absorption wavelength of the component of interest. This method makes it possible to image selective materials, e.g. hemoglobin, lipid, water etc. [2]. Selective photoacoustic imaging of different tissues especially comes in handy for cancer imaging, since blood oxygenation, and thus the absorption of hemoglobin, is different in tumors compared to the surrounding tissue [2]. Selective imaging makes it possible to detect tumors, and also decide their size and location in the body. The graph in figure 1.2 shows the absorption coefficient as a function of wavelength for different light absorbers of biochemical interest [4]. In addition, the introduction of biomarkers further increases the ability to detect cancer earlier and more exactly [7]. Biomarkers include differ-
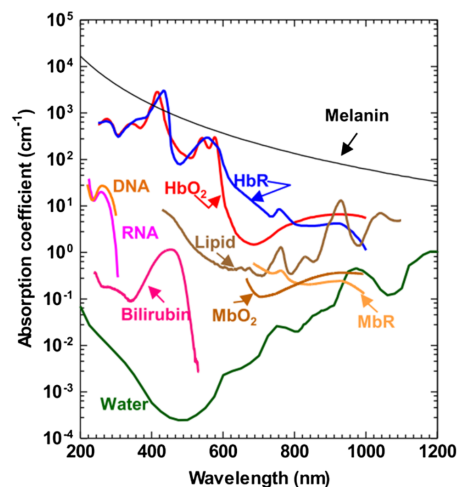
Figure 1.2: The absorption coefficient as function of wavelength for different biological materials, including DNA/RNA, hemoglobin (both oxygenated and de-oxygenated), melanin, lipid and water. Image from [4]

ent contrast agents or dyes with known absorp-
tion capabilities [7], which can be injected into
the body to "target" areas of interest.

It is possible to achieve a range of spatial resolutions and imaging depths from different setups
of lasers, ultrasonic transducers and scanning mechanisms. Photoacoustic imaging can be roughly
divided into two different methods, namely photoacoustic microscopy (PAM) and photoacoustic
computed tomography (PACT) [4]. Photoacoustic microscopy consist of single-element ultrasonic
detection and generates an image directly through a scanning mechanism. Meanwhile, PACT have
multi-element ultrasonic detection and uses inverse image reconstruction [7]. Further more, PAM
has shorter penetration depth than PACT, but better image resolution [7]. The next section is
dedicated to PAM and its modes.

1.2   Photoacoustic Microscopy

Photoacoustic microscopy involves imaging techniques where an image is created using either a
focused ultrasonic transducer or a focused laser beam. Thus, PAM may be separated into two
separate modes; acoustic-resolution photoacoustic microscopy (AR-PAM) and optical-resolution
photoacoustic microscopy (OR-PAM). As the names imply, AR-PAM include systems where the
ultrasound transducer is focused while OR-PAM covers systems utilizing a focused laser beam.

1.2.1   Acoustic-Resolution Photoacoustic Microscopy

Acoustic-resolution photoacoustic microscopy includes imaging techniques where the photoacoustic
signals are detected by a single focused ultrasonic transducer [2]. The transducer is either mechani-
cally translated or rotated around the object. Figure 1.3 shows an example of a set up for AR-PAM.
The UT is placed above and focused on the object of interest, while the laser light is directed around
the UT and weakly focused at the object [2]. Such an optical focus is not essential for AR-PAM,
as it has no effect on the spatial resolution. The length scale of AR-PAM is not definite, it can be
adjusted to fit the desired depth. E.g. if the bandwidth is reduced and the focal length is increased,
the resulting imaging depth will be increased [2]. A larger imaging depth, however, comes at the
expense of reduced spatial resolution.
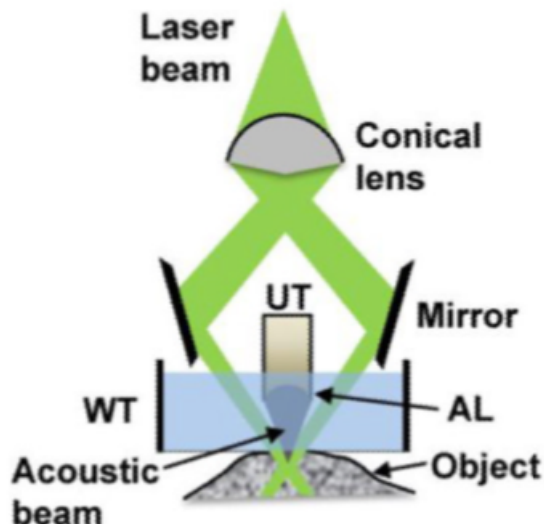
Figure 1.3: Acoustic-resolution photoacoustic microscopy (AR-PAM), the lateral resolution is defined by the acoustic focusing achieved by the acoustic lens. AL: acoustic lens, UT: ultrasound transducer, WT: water tank. Image from [2].

1.2.2   Optical-Resolution Photoacoustic Microscopy

The optical-resolution mode include imaging systems where a focused laser beam is utilized. An example set-up is shown in figure 1.4. The focused laser defines the lateral resolution obtainable for the image [8]. Due to optical scattering, it is only possible to obtain superficial images using this technique. For most tissues, the laser light can penetrate a maximum distance of approximately 1 mm [8]. Beyond this limit, scattering of the laser light causes the beam to defocus and thus reduces the resolution [8]. Because of the high lateral resolution obtainable in OR-PAM, it is possible to image both individual capillaries and individual red blood cells in the mouse ear [8].

Furthermore, there are different options when placing the laser and transducer with regards to the imaging target. The laser and transducer can be either placed on the same or opposite sides of the object to be imaged. When the laser is placed on the same side as the transducer, the laser light is absorbed by the object and reflected from it as an acoustic wave. Thus, this set-up is named the reflection mode PAM. For the second set-up, the laser light is absorbed by the object on one side and emitted as an acoustic wave on the other side. Hence, this set-up is called the transmission mode PAM. See figure 1.5 for both reflection and transmission mode. Additionally for the reflection mode, there are several ways to position the laser relative to the transducer. E.g. the light from the

laser may be directed around the transducer by using lenses, as in figure 1.3. Or, the laser could be placed in an angle relative to the transducer or going through the transducer [9] as shown in figure 1.5. Both AR-PAM and OR-PAM exists in these two modes.
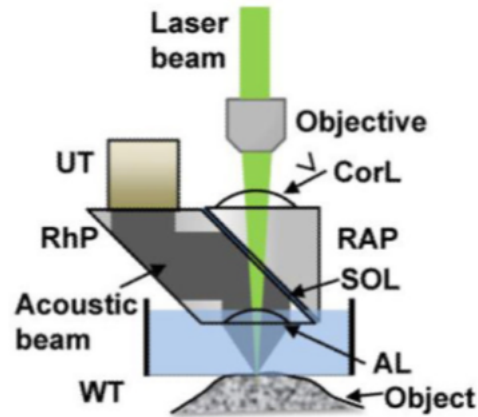
Figure 1.4: Second-generation optical-resolution photoacoustic microscopy (G2-OR-PAM), the laser beam is tightly focused by the correction lens. AL: acoustic lens, CorL: correction lens, RAP: right angled prism, RhP: rhomboid prism, SOL: silicone oil layer, UT: ultrasonic transducer, WT: water tank. Image from [2].
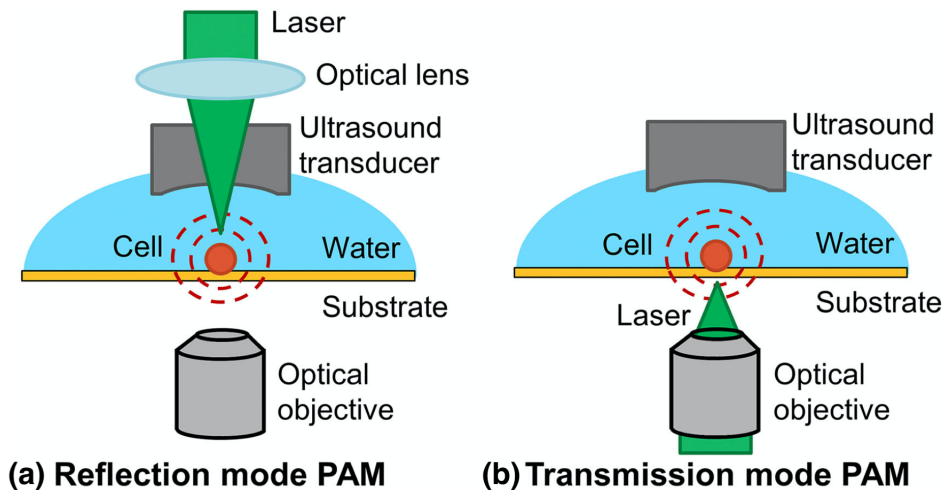
Figure 1.5: Figure showing two different modes of PAM. (a) Reflection mode, where the laser and the transducer is placed on the same side of the object to be imaged. (b) Transmission mode, where the laser and the transducer is placed on opposite sides of the object. Image from [9]

Chapter 2

Theory

2.1 Elasticity

The elasticity of an object refers to its ability to revert to its original shape and size after being deformed by a force [10]. Hooke's law says that the extension experienced by an elastic object is directly proportional to the force that is applied to it, which may be generalized to say that stress is proportional to strain. Here, strain denotes the relative change in a spatial dimension (length, angle or volume) and stress is the applied force per unit area causing this deformation [10]. Furthermore, the coefficient named the elastic modulus relates a type of stress to the strain it causes. There exists three basic types of stress, and thus three different elastic moduli; Young's modulus, shear modulus and bulk modulus [10]. Young's modulus describes a materials response to stress applied normal to opposite faces [10], and is often referred to as the elastic modulus, E [11]. The higher value of E, the stiffer a material is.
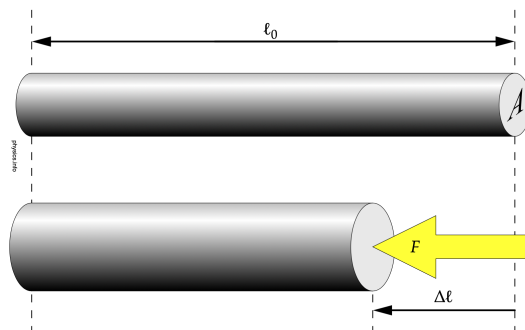
Figure 2.1: Figure demonstrating the elasticity of an object. The force F compresses the object by a length Δl, if the object is perfectly elastic. When the force is removed the object will revert back to its original length l_0. Image from [10].

2.2 Ultrasound Waves

Ultrasound (US) waves are the sound waves that propagate through a medium with frequencies above 20 kHz [1], i.e. higher than what can be perceived by the human ear. Normally, an ultrasonic transducer is used to produce and record the US waves. However, in PAM the waves begin to propagate due to vibrations in the tissue caused by heating. Heating is caused by optical light incident on the tissue. A transducer is used to record these waves. Then, the signal is converted into an image through different algorithms [8].

Sound waves, and thus ultrasonic waves, exist in several different *modes*. These modes denote the different patterns a wave may propagate in [12]. In ultrasound, mostly longitudinal and transverse (shear) waves occur. Longitudinal waves travel parallel to the propagation direction of the wave, whereas transverse waves travel perpendicular compared to the wave direction [12]. In addition, surface (Rayleigh) waves and Lamb waves occur at surfaces and interfaces [12]. Surface waves appear as elliptically shaped waves, consisting of both a longitudinal and a transverse part [13], as shown in figure 2.2. As the name implies, surface waves propagate along the surfaces of solid materials [12; 13]. Since surface waves follow the curvature of an object, they become useful when detecting small details in the surface, which other wave modes are unable to detect [13].
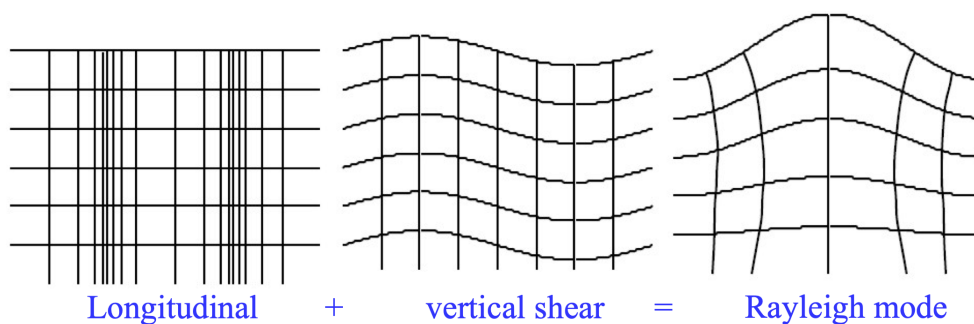
Figure 2.2: The Rayleigh mode, or surface wave, which consists of both a longitudinal and a vertical component. The direction of travel is defined in the horizontal direction. Image from [13].

2.3 FWHM and Percent Bandwidth

Full-width at half-maximum is used to measure the width of a peak of a function, e.g. the one included in Figure 2.3. To calculate the FWHM in terms of wavelength, the frequency bandwidth at half maximum must be measured first. This is equal to $f_+ - f_-$ in the figure. An equation valid for small intervals of wavelength [14] can be used to convert the bandwidth from frequency to wavelength;

$$\Delta\lambda = \Delta f \frac{c}{f_c^2}, \tag{2.1}$$

where c is the sound velocity in the material and f_c denotes the center frequency of the peak. The percent bandwidth, $\%BW$, is calculated from the frequency bandwidth and the center frequency using that

$$\%BW = \frac{BW}{f_c} = \frac{f_+ - f_-}{f_c}. \tag{2.2}$$

The bandwidth is found from the upper and lower frequencies, f_+ and f_-, where the amplitude is at half maximum.
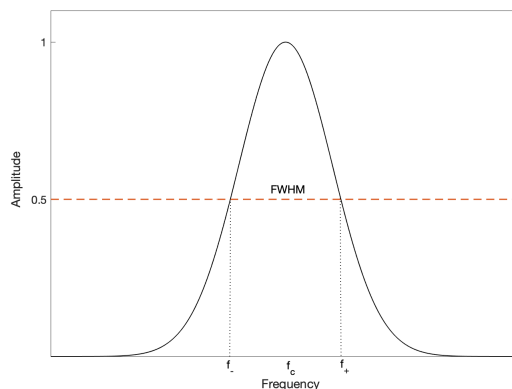
Figure 2.3: The FWHM of a function.

2.4 Spatial Filtering

When a laser beam is produced by its source it does not have a smooth intensity profile [15]. Thus, a spatial filter can be applied to remove unwanted peaks of energy, only keeping the central maximum of the diffraction pattern [15]. Furthermore, dust located in the air or on the components of the setup may scatter the laser beam which causes ring patterns in the beam profile [15]. The spatial filter removes this noise as well from the signal [16]. The spatial filter consisted of an aspheric lens, a pinhole and a collimating lens. The setup is illustrated in Figure 2.4. When the beam is focused by the aspheric lens, it is transformed into a Gaussian spot, however with side fringes representing unwanted energy [16]. These side fringes are removed from the signal when it travels through the pinhole, leaving only a clean Gaussian spot [16]. Lastly, the signal goes through a second lens which collimates it.
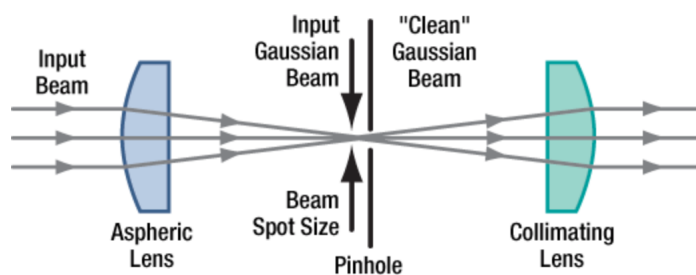
Figure 2.4: A spatial filter system, consisting of two lenses and a pinhole. Image from [16].

2.5 Reflection and Transmission Coefficient

When an US wave interacts with a boundary between two materials of different acoustic impedances (Z), it is reflected [17]. The difference in Z is often referred to as an impedance mismatch [17]. The percentage of energy reflected from the boundary is dependent on this mismatch; a greater mismatch yields a higher percentage of reflected energy [17]. The fraction of the incident wave intensity reflected from the boundary can be calculated from the equation given below. This is known as the *reflection coefficient*, and multiplied by 100 gives the reflected energy amount in percent [17]. For normal incident, the reflection coefficient of the wave energy is given by

$$R = \left(\frac{Z_2 - Z_1}{Z_2 + Z_1}\right)^2,$$

(2.3)

where Z_1 is the acoustic impedance in the first material and Z_2 is the acoustic impedance in the second material. As the reflected energy plus the transmitted energy equals the total amount of incident energy, the transmission coefficient T can be found by subtracting the reflection coefficient from one;

$$T = 1 - R.$$

(2.4)

2.6 Heat Diffusion Equation

The heat diffusion equation is a partial differential equation that explains how the temperature in a material varies over time [18]. It can be expressed as

$$\rho C_p \frac{\partial T}{\partial t} = \nabla(k\nabla T) + Q,$$

(2.5)

where ρ is the mass density, C_p is the heat capacity with constant pressure, k is the thermal conductivity and Q denotes the external heat source, which in this case is the laser beam. The term $\nabla(k\nabla T)$ represents the heat flux through the material.

2.7 Equations Explaining Heating of Tissue

The equations and explanations given in this section were obtained from the review paper by Zhou Y. et al. [4].

Absorption of laser light in tissue leads to an increase in the local temperature. The temperature increase causes a rise in the local pressure, which in turn produces a propagating acoustic wave. In this section, the equation describing how the pressure increase due to a rise in the temperature are derived.

First, the thermal relaxation time, τ_{th}, and the stress relaxation time, τ_s, can be expressed as

$$\tau_{th} = \frac{d_c^2}{\alpha_{th}} \tag{2.6}$$

and

$$\tau_s = \frac{d_c}{v_s}, \tag{2.7}$$

where d_c is the desired spatial resolution, α_{th} is the thermal diffusivity (m^2/s) of the material, and v_s is the speed of sound (m/s) in the material. When the laser excites the tissue, it leads to an expansion of the volume, dV/V. This expansion can be expressed by the following equation

$$\frac{dV}{V} = -\kappa p + \beta T, \tag{2.8}$$

where κ is the isothermal compressibility (Pa^{-1}) of the material, p is the change in the pressure (Pa), β is the thermal coefficient of the volume expansion (K^{-1}) of the material and T is the *change in temperature* (K).

If the duration of each laser pulse is shorter than τ_{th} and τ_s, the condition of thermal and stress confinement is fulfilled. Consequently, the volume expansion dV/V is negligible and an expression for the pressure rise, p_0, may be derived from equation 2.8

$$p_0 = \frac{\beta T}{\kappa}. \tag{2.9}$$

The local temperature rise induced by the laser excitation can be expressed as

$$T = \frac{\eta_{th} A_e}{\rho C_v},$$

(2.10)

where η_{th} represents the percentage of the absorbed light that is converted into heat, A_e is the specific optical energy deposition (J/m^3), ρ is the density of the tissue and C_v is the specific heat capacity at constant volume. Equation 2.10 can be substituted into equation 2.9 to obtain

$$p_0 = \frac{\beta \eta_{th} A_e}{\rho C_v \kappa}.$$

(2.11)

The dimensionless Grüneisen parameter, Γ, is defined as $\frac{\beta}{\rho C_v \kappa}$. Thus, equation 2.11 may be simplified to

$$p_0 = \Gamma \eta_{th} A_e.$$

(2.12)

For single-photon absorption, one photon excites an atom to a higher energy state. Then, the energy deposition, A_e, is proportional to the optical fluence (intensity) F (J/cm^3) so that

$$p_0 = \Gamma \eta_{th} \mu_a F,$$

(2.13)

where μ_a is the optical absorption coefficient, which determines how far into the tissue the light can penetrate before it is absorbed. Equation 2.13 suggests that the pressure rise is proportional to μ_a and F. Normally, Γ and η_{th} are assumed to be constants. Hence, if p_0 can be measured and F is known it is possible to obtain a value for μ_a.

Chapter 3

Experimental method

To be able to benchmark and model the system, non-biological PAFs with well-known material properties were used for experiments and simulations. In this chapter the experimental setup and scanning method will be presented, along with the method used to fabricate the PAFs.

3.1 Experimental Setup

Transmission mode optical-resolution PAM was the imaging method used for the experiment. A diagram explaining the setup is included in Figure 3.1. For scanning and recording data, a Leica DMI8 Inverted Microscope was used. The microscope was integrated with an ASI MS-2000 XYZ High Precision scanning stage. The scanning parameters and position of the stage was managed in LabVIEW, which also displayed the resulting photoacoustic images. Scanning was executed at room temperature.

A 532 nm pulsed laser was used as the light source. It had a pulse width of 2 ns and a repetition rate of 10 kHz. The energy was specified as 20 μJ, thus the peak power could be calculated from

$$Peak\ power\ (W) = \frac{Energy\ per\ pulse\ (J)}{Pulse\ width\ (s)} = \frac{20\mu J}{2ns} = 10kW. \tag{3.1}$$

Laser specifications are included in Appendix C. After being emitted, the laser beam was transmitted through an optical isolator which ensured that no back reflections were hitting the laser

source. A neutral density filter was added as well, to reduce the laser beam power. Then, a beam splitter redirected a small portion of the light to a photodiode which triggered the system. Lens 1 and 2 and the pinhole worked as a spatial filter, collimating the beam and reducing noise. The light from the laser was focused onto the sample by an optical objective with 10x magnification and numerical aperture of 0.3. The optical light that is not absorbed and reflected back from the sample passes through the objective lens and the second beam splitter to a tube lens and then to an optical camera. This facilitates real-time optical imaging of the sample in reflection mode as an additional non-PAM imaging modality in system.

Figure 3.2 includes a diagram of the transducer and laser in a transmission mode PAM setup. The PAF consisted of polydimethylsiloxane (PDMS) mixed with black toner particles, originally used in laser printing. Polydimethylsiloxane is a silicone-based polymer widely used for coating and more [19]. The solution was spin coated onto a polymer petri dish working as a sample holder, before being placed on the scanning stage. A polymer petri dish was chosen to avoid laser light being reflected off of it, as it would for a glass dish. The polymer dish had a refractive index of $n_D = 1.52$. The approach for fabricating the PAF is thoroughly explained in Section 3.2. The petri dish was then filled with distilled water for the US waves to propagate through. Note that the thickness of the PDMS coating in proportion to the petri dish is not to scale in the figure. The petri dish had a 50 mm diameter and thickness of 180 μm, other specifications for the petri dish are included in Appendix A. The laser source was placed underneath the sample and focused onto the bottom of the PAF by an optical objective. The US waves generated by the sample were received by a 50 MHz PVDF transducer immersed in the water. Using a high-frequency transducer ensured a high spatial resolution, but a limited imaging depth. The transducer frequency response is included in Appendix B. Finally, the resulting photoacoustic images were presented directly on a display monitor by software written in LabVIEW.

Some acoustic properties for PDMS, polystyrene, water and air are listed in Table 3.1. Since the exact material of the petri dishes are not revealed, values for polystyrene were used as substitutes. Note that values for PDMS are for the "clean" material, and does not take into account the toner particles. Values for air, PDMS and the sound speed in water were gathered from [20], for the acoustic impedance of water the value given in [21] for 20° was used. The values for polystyrene were found at [22] and [23], respectively.

Table 3.1: Acoustic properties of air, water, PDMS and polystyrene.

	Air	Water	PDMS	Polystyrene
Sound speed (m/s)	334	1490	1119	2350
Acoustic impedance (MRayls)	0.000401	1.48	1.08	2.52
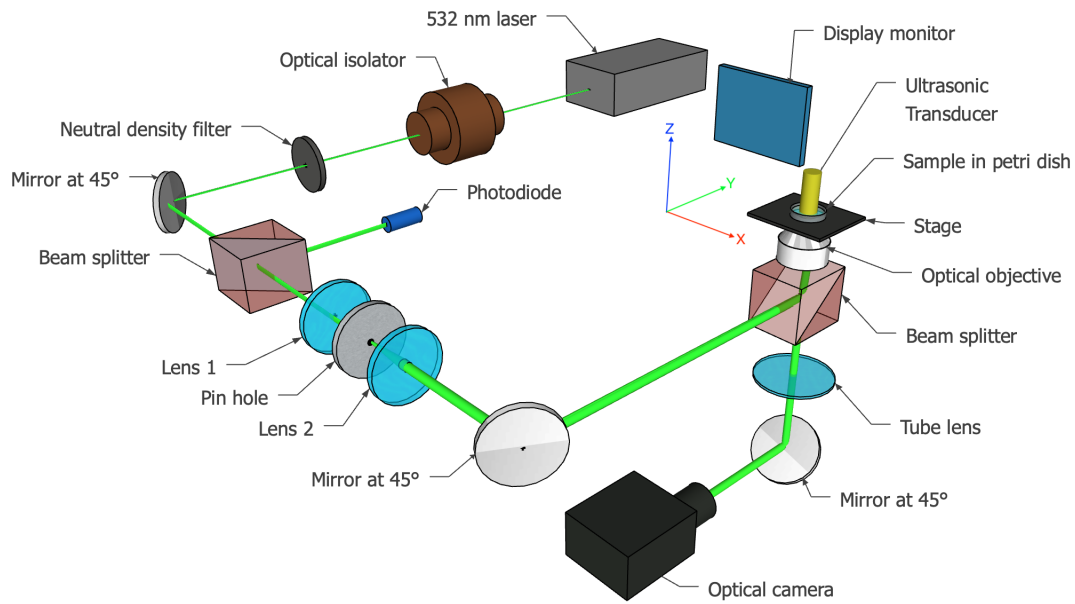
Figure 3.1: Diagram of the experimental setup. The laser light was spatially filtered to collimate the beam, and then focused onto the PAF by an optical objective of 10x magnification.
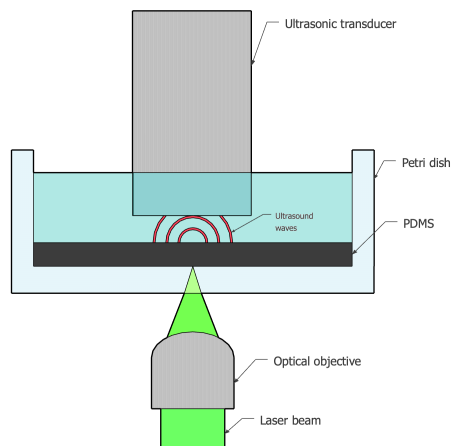
Figure 3.2: Illustration of the setup of the transducer and laser, utilizing transmission mode PAM to produce ultrasound waves.

3.2 Fabricating the PAF

To increase the amount of laser light absorbed by the PDMS, it was mixed with black toner particles obtained from the ink cartridge for a laser printer. The size of the particles was on the nanoscale. In order to achieve a satisfactory blend between the two components, the toner powder was first mixed with a PDMS crosslinker of lower viscosity. After blending thoroughly by hand, a PDMS base with higher viscosity was added. The mixing ratio used was 1(crosslinker):10(base). Then the solution was placed in a vacuum chamber to remove any air bubbles in it. Afterwards, a spin coater was used to create an even coating on the surface of the petri dish. Figure 3.3 includes some images captured in the laboratory. The top right image is of the petri dish with a small amount of the PDMS solution placed on top of it, taken before spin coating. The bottom image shows two petri dishes spin coated at 4000 RPM for approximately 1 minute. A lower RPM was used for the first few rotations to avoid throwing the solution off of the petri dish, thus ensuring a thicker coating.

Two different PAFs with solutions consisting of different amounts of toner particles were made. They are imaged in the bottom of Figure 3.3. Both solutions included approximately 0.5 grams of crosslinker to 5 grams of base, but a) had 1 gram of toner while b) had 0.5 grams of toner. The difference in saturation was significant, as seen in the image. Looking closely it was possible to observe some clusters of the black toner particles in the coating. Clustering of nanoparticles into larger micro-clusters is a known problem which probably could have been reduced by developing the blending approach further, e.g. by doing it mechanically instead of by hand. After spincoating, the PAF was crystallized by placing the petri dishes on a heat plate holding 40°C overnight. Ideally, the coating would crystallize at 90°C in one hour, but due to the polymer in the petri dishes only being temperature-stable up to 80°C this solution was chosen instead.
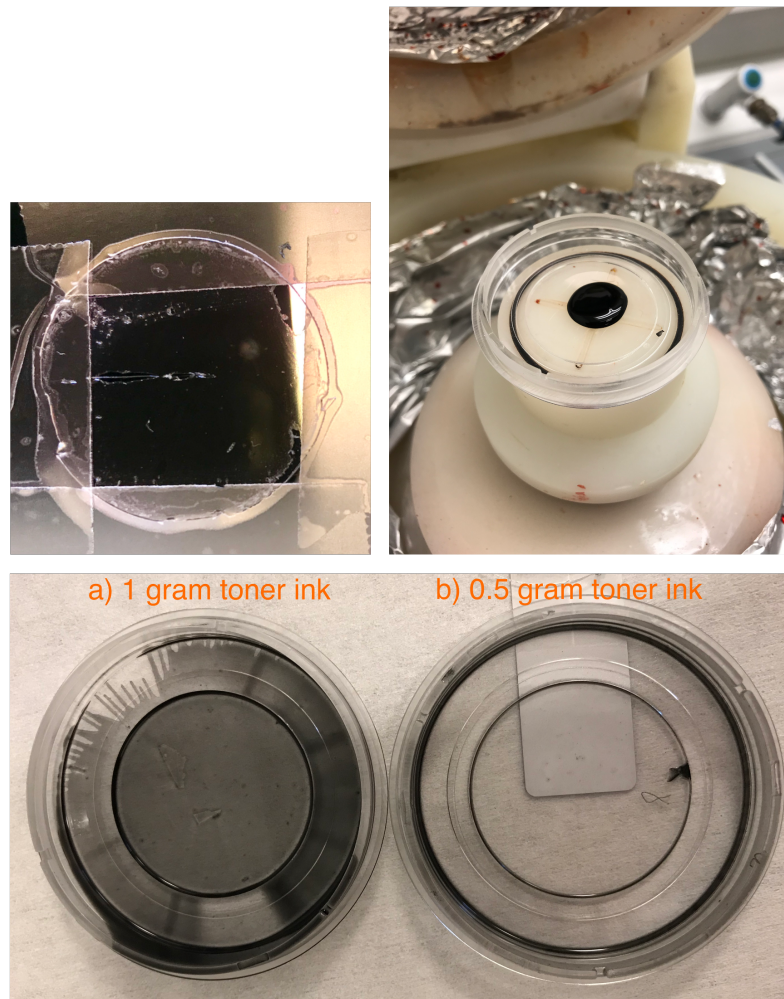
Figure 3.3: [Top left] A scraped sample used to determine the thickness of the PDMS layer through nano profiling. [Top right] A petri dish with a small amount of the PDMS solution, before spin-coating. [Bottom] After spincoating of two different mixing ratios of toner ink; a) had 1 gram of toner ink, while b) had 0.5 grams of toner ink to the same amount of PDMS.

3.2.1 Nano Profiling

A nano profiler was used to determine the thickness of the PAF. The top left image in Figure 3.3 shows the sample which was placed in the profiler; the bottom of the petri dish was cut out and taped onto a plate. Some of the coating was scratched off using a thin needle, and the nano profile was taken across the cut. Figure 3.4 includes the resulting profile, taken over a distance of 1 mm. The cut was visible between approximately 0.35 mm and 0.67 mm. Notice the additional cut located at 0.5 mm, where the needle scraped the petri dish as well. From the nano profile the thickness of the PDMS coating on this sample was estimated to be between 12 and 13 μm. The uniformity of the PAFs surface could also be investigated from the nano profile. On the left side of the cut, it was smoother and had a maximum difference between top and bottom of approximately 3 μm. On the right side, it was more serrated and had a maximum difference of 5 μm. The serrations may be caused from scraping the needle over the sample, which pushed the excess film to the sides causing the surrounding areas to scrunch up.

Figure 3.5 includes plots illustrating the relationship between the thickness of a PDMS coating and the RPMs. In addition, the thicknesses for 1000 RPM and 6000 RPM as functions of spin time are included. The thickness of the coating decreased exponentially with both the spincoating speed and the total time of spincoating. The PAF coating used in the experiment was spincoated at a lower RPM first to ensure a thicker film layer. Moreover, the PAF included toner particles that may impact how the solution spread out. Thus, there was some deviation between the plots and the results obtained from the nano profile.
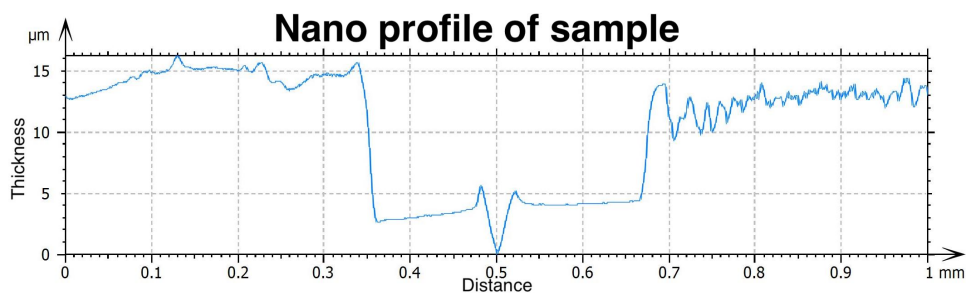
Figure 3.4: Nano profile of a sample spincoated at 4000 RPM. The thickness of the PAF was estimated to be between 12 and 13 μm.
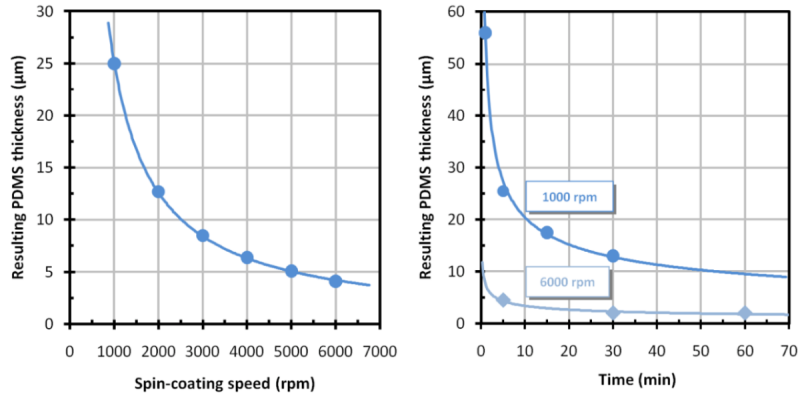
Figure 3.5: [Left] PDMS thickness as a function of spin speed (RPM). [Right] PDMS thickness for two different RPMs, as function of time. Image from [24].

3.2.2   Absorption Coefficient

Since the PAF was made with a solution consisting of two components, i.e. PDMS and black toner particles, the actual absorption coefficient was not known. However, the absorption coefficient of pure PDMS exists in literature. A plot of the absorption coefficient of PDMS as a function of the wavelength of the incident optical light is included in Figure 3.6. For a laser with a wavelength of 532 nm, the absorption coefficient of PDMS is approximately 1.5 cm^{-1}. For a combination of PDMS and black toner particles the absorption coefficient would be higher than this by some amount.
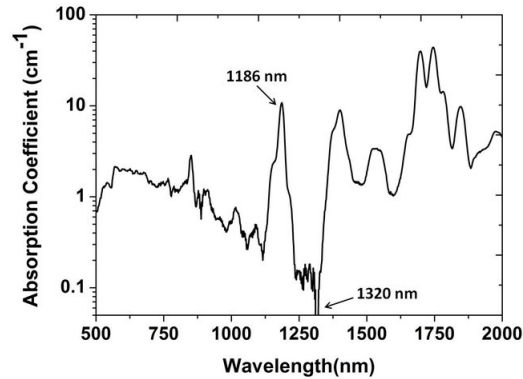
Figure 3.6: Absorption coefficient of PDMS as a function of the wavelength of the incident optical light. Image from [25].

3.3 Imaging Optimization

Several steps were taken to ensure that the quality of the resulting photoacoustic image was optimized. To optimize the alignment of the transducer and the laser beam, an arbitrary sample containing microparticles was placed on the scanning stage. Microparticles were used because they are easier to distinguish from each other compared to nanoparticles. First, the transducer was focused by adjusting its position step wise in the z-direction and searching for the maximum amplitude of the received signal. For each step, the transducer was displaced by 0.5 mm. Finding the maximum ensured that the sample was located in the transition between the near field and far field of the transducer. After focusing the UT, it was aligned with the laser beam by manually adjusting the microscope until the produced image lined up with the path of the laser. This was confirmed only by manually observing the produced acoustic image. Finally, the petri dish containing the PAF was inserted into the system. When changing samples, the transducer had to be raised out of the water. After immersing it again, it was important to remove any bubbles of air trapped on the underside of the transducer which could affect the quality of the photoacoustic image.

The photoacoustic scan was taken at a speed of 0.25 mm/s in both the x- and y-direction. Low speed ensures that the transducer has time to receive the signal for each step, producing a higher quality image. A high averaging of 64 times was used to reduce noise in the images.

3.4 Cross Correlation in MATLAB

A future goal with the PAFs, is to use them for phase imaging. Since correlation methods are very important for phase imaging, this section will look at a method to determine the phase shift between two signals from the cross correlation. Cross correlation takes two input signals and produces a third signal [26], which is the measurement of how well the input signals match each other for each time step. The higher the value, the better the match. To investigate the method, the cross correlation between a Gaussian pulse train and three phase shifted waveforms were calculated in the frequency domain in MATLAB. The phase shifted waveforms were another Gaussian pulse train, and the first and second derivatives of this pulse train. All the signals were normalized to their respective peak value, and the pulse trains were defined so that they were infinitely repeatable. Further, the vectors defining the pulse trains contained 2048 values, as the time signals generated from the experiment would.

The built-in MATLAB function circshift() were used to shift the signals by 60 time steps to the right. To find the cross correlation, the discrete Fourier transform were taken of both input signals.

The Fourier transform of the second input signal was then complex conjugated and multiplied with the Fourier transform of the first input signal. Then, the inverse discrete Fourier transform operation was applied to the resulting signal. This signal contained the cross correlation between the two input signals, and was plotted as a function of the lags it was calculated for.

Figure 3.7 includes both plots of the Gaussian pulse vs. the shifted pulses and their respective cross correlation calculated for the Fourier domain. The cross correlations were in the shape of a pyramid, where the lag corresponding to the peak value denoted the time shift needed to obtain the best match between the waveforms. Note that the 2nd derivative Gaussian had two peaks, and thus two lags corresponding to the best match.

Cross correlation gave the shift in amount of time steps, to figure out the time delay it was multiplied with the length of one time step. From this time delay, the phase shift in degrees could be found from

$$ps = 360\frac{td}{P}, \tag{3.2}$$

where ps = phase shift, td = time delay and P = wave period. Since the pulse trains were defined to last for $t = 5.12\mu s$ and contained $N = 2048$ samples, one time step was equal to $td = t/N = 2.5$ ns. The pulse train contained four peaks, evenly spaced out over the signal. Thus, the wave period was $2048/4 \cdot td = 1.28\mu s$. The phase shifts obtained for the largest cross correlations of the three different cases have been included in Table 3.2. For the 2nd derivative Gaussian pulse train, the shortest lag was chosen. The sign of the phase shift denotes if it is shifted to the left (+) or right (-) with respect to the main Gaussian pulse train.

For the experiment, the signals would experience small time delays from travelling through the PAF and the water. Some noise would be arising from the electronic instruments included in the setup as well, which could lead to uncertainties of the cross correlation results. The repetition rate of the pulsed laser was used to find the wave period when calculating phase shift of the experimental results. Since the laser pulse had a repetition rate of $f_r = 10$ kHz, the wave period was $P = 1/f_r = 100\mu s$.

Table 3.2: The lag for the highest cross correlation and its corresponding phase shift, for three arbitrary cases in MATLAB.

	Lag (abs)	Phase shift (°)
Gauss vs. Gauss	-60	-42.2
Gauss vs. 1st der.	-3	-2.1
Gauss vs. 2nd der.	38	26.7
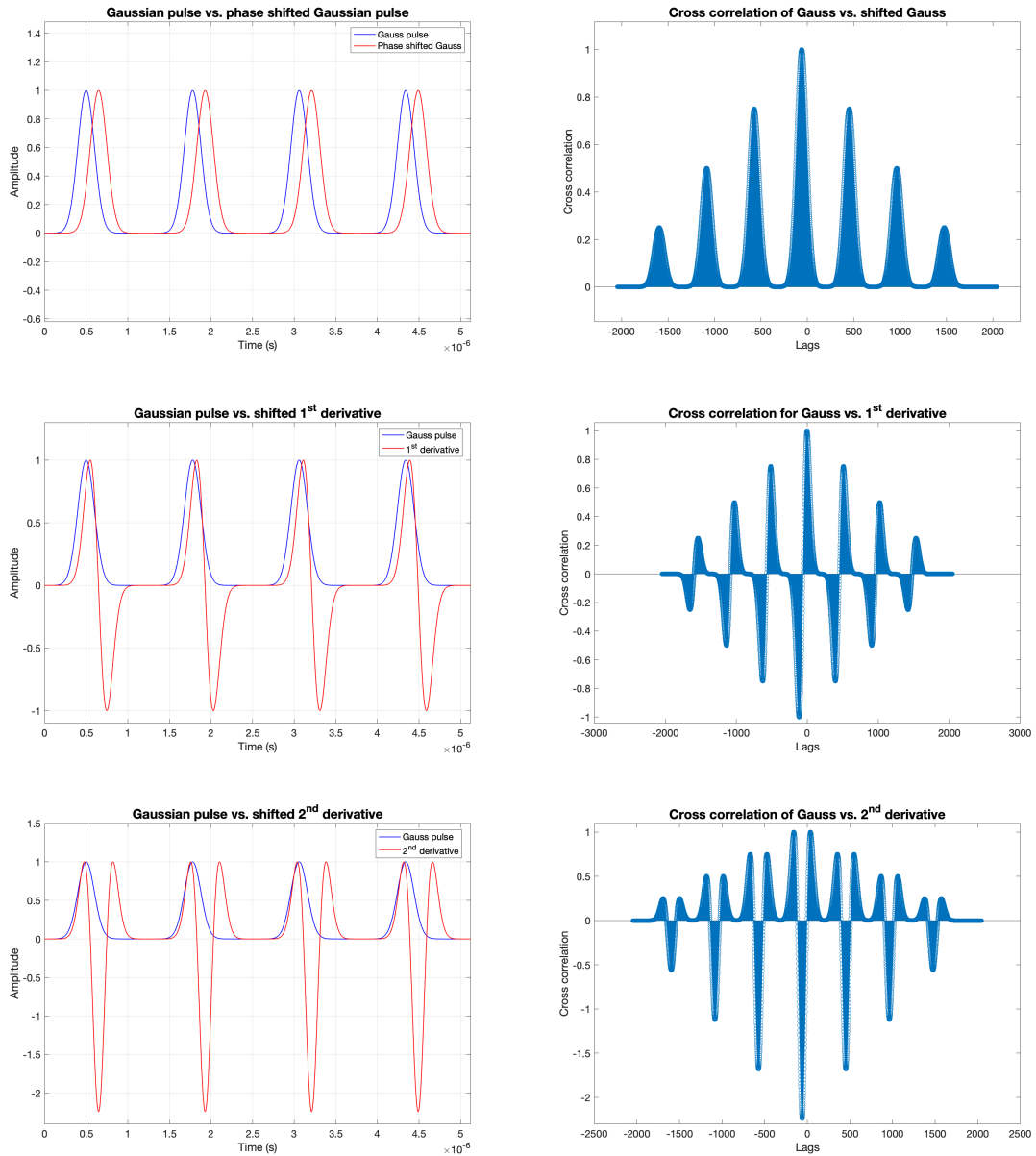
Figure 3.7: The cross correlation in the Fourier domain was calculated for three arbitrary cases; Between the Gaussian pulse train and the phase shifted Gaussian pulse train, and the 1st and 2nd derivative of the phase shifted pulse train. All waveforms were shifted by 60 timesteps to the right.

Chapter 4

COMSOL simulation

The goal of the COMSOL simulations was to explore how physical parameters such as film thickness, its absorption coefficient and laser beam width affected the results. To simulate the PAF, a layer of PDMS with an adjustable absorption coefficient was used. Increasing the absorption coefficient was equivalent to adding more toner particles to the coating.

4.1   Global parameters

To conduct the numerical investigation of a PAF, the experimental setup explained in Section 3.1 was simulated in COMSOL Multiphysics. Table 4.1 gives an overview of the global parameters used to define this model. Some of the parameter values were later adjusted for analytical purposes.

Table 4.1: The global parameters used in the COMSOL model.

Name	Expression	Description
I0	1E6 [W/m^2]	Laser intensity
mu0	1/40 [1/μm]	Absorption coefficient
si0	5 [μm]	Width of laser beam
si0t	10 [ns]	Length of laser pulse
T_pdms	30 [μm]	Thickness of PDMS layer
T_dish	180 [μm]	Thickness of petri dish
T_water	400 [μm]	Thickness of water layer
W	250 [μm]	Width of section to model
Tref	293.15 [K]	Reference temperature
p_tran	24 [μm]	Thickness of piezofilm
w_tran	200 [μm]	Transducer aperture width
b_tran	50 [μm]	Thickness of backing

4.2 Beer-Lambert law

To implement the interactions between the laser and the material in COMSOL, the Beer-Lambert law was applied [27]. This law describes the absorption of laser light in a material [27]. The model can be used with some assumptions, namely that the light is monochromatic, collimated, and experiences minimal reflection, refraction and scattering while interacting with the material [27]. The Beer-Lambert law can be written as

$$\frac{\partial I}{\partial z} = \mu_a I, \tag{4.1}$$

where I is the light intensity and μ_a is the absorption coefficient. Normally, the absorption coefficient would be dependent on the temperature of the material. However, as the temperature increase was presumably small it was assumed to be independent of it. Due to the small variations in temperature, the partial differential equation for the temperature distribution had to be solved as well [27]. This equation equals the heat diffusion equation in 2.5, except that $Q = \mu_a I$;

$$\rho C_p \frac{\partial T}{\partial t} - \nabla(k\nabla T) = \mu_a I. \tag{4.2}$$

As before, $\nabla(k\nabla T)$ denotes the heat flux. Due to thermal confinements the flux term is set to zero, giving

$$\rho C_p \frac{\partial T}{\partial t} = \mu_a I. \tag{4.3}$$

To implement this in COMSOL, the *Coefficient form PDE* was used. It gave a partial differential equation of the form

$$e_a \frac{\partial^2 U}{\partial t^2} + d_a \frac{\partial U}{\partial t} + \nabla(-c\nabla U - \alpha U + \gamma) + \beta \cdot \nabla U + aU = f, \tag{4.4}$$

where all the coefficients could be specified manually. U represents the dependent variable, e.g. temperature, intensity etc. For the Beer-Lambert equation for the temperature T, all coefficients were set equal to zero, except for f and d_a;

$$f = mu0 \cdot I0 \tag{4.5}$$
$$d_a = material.rho \cdot material.Cp. \tag{4.6}$$

The dot-notation acquired the density and heat capacity for constant pressure from the material database, which caused it to equal equation 4.3. To model the intensity, another Coefficient form PDE was implemented where all coefficients except f were set to zero. The parameter f was defined as

$$f = Inz + mu0 \cdot In. \tag{4.7}$$

In represented the intensity, and Inz its derivative with respect to z. Thus,

$$\frac{\partial I}{\partial z} = -\mu_a I. \tag{4.8}$$

Together, the two equations gave a relation between the intensity of the laser and the temperature increase in COMSOL.

4.3 Creating the model

The model simulated a cross section of a small part of the setup. In the bottom a polystyrene slab was placed, which had material properties similar to the polymer petri dishes used in the experiment. On top of this, a layer of PDMS was added to function as the PAF. The material parameters for PDMS were manually selected, using information found in [28] and table 1 in [29]. These values are listed in table 4.2. It should be noted that the toner particles included in the actual PAF were not taken into account when choosing these values. Finally, a thicker layer of water was added for the acoustic waves to propagate through. The laser was implemented as a boundary condition, which will be explained in more detail in a later section. Figure 4.1 shows the cross section of the model, which was symmetric around the axis at r=0. The section had a radius of 250 μm. The petri dish had a thickness of 180 μm, while the PDMS layer on top was 30 μm thick. The thickness of the water layer was set to 400 μm. All boundary conditions, which are defined later, are included as well in Figure 4.1.

Table 4.2: Material parameters used to simulate PDMS.

Property	Variable	Value
Density	rho	970 [kg/m^3]
Poisson's ratio	nu	0.4999 [1]
Young's modulus	E	1.32e6 [Pa]

As mentioned, the model was supposed to represent a small section of the actual setup. Thus, it was desirable to simulate that a larger area surrounded the section in the model. To do this, a spherical reflection boundary was implemented on the outer edges of the water layer, as shown in figure 4.1. This boundary condition ensured that the reflections from the edges were small, simulating a larger body of water existing beyond the boundary. In practice, this edge did not exist since the petri dish was much larger (50 mm in diameter).

The laser beam was modelled as a Gaussian pulse with a standard deviation of 10 μm, named Ldis(r). Likewise, the pulse function ft(t) was also modelled as a Gaussian pulse with a standard deviation of 10 ns. Both Ldis(r) and ft(t) are plotted in figure 4.2. To be able to resolve the ultrasonic waves, a mesh with maximum and minimum element size of 10 μm and 5 μm, respectively, was chosen. The mesh grid may be viewed in figure 3.7.
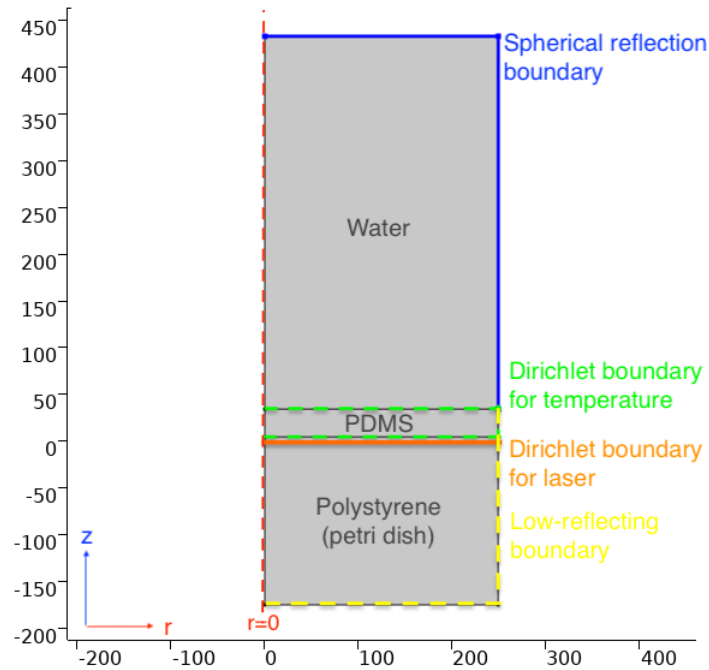
Figure 4.1: A model for simulating heating of PDMS by laser light, and the induced acoustic waves. The placements of all boundary conditions defined for the model were included. Blue: spherical reflection boundary, green dotted: Dirichlet boundary regarding temperature, orange: Dirichlet boundary regarding laser intensity, yellow dotted: low-reflecting boundary. Axial symmetry around r=0.
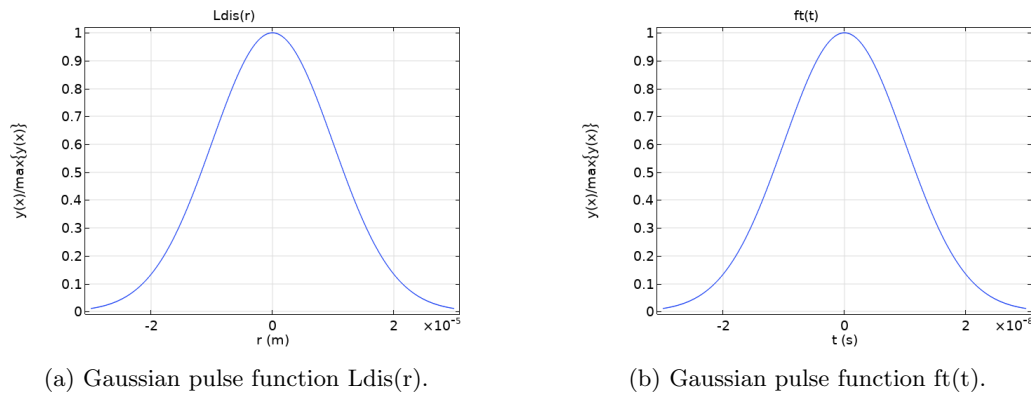
(a) Gaussian pulse function Ldis(r).

(b) Gaussian pulse function ft(t).

Figure 4.2: Plot of the two Gaussian pulse functions explaining the (a) spatial and (b) temporal parts of the laser pulse. Both functions were normalized.

4.3.1 Body Load

The tensor relations between stress and strain for an isotropic, linear elastic solid [30] where ϵ_{ij} and σ_{ij} represent the strain and Cauchy stress tensor, respectively, is

$$
\begin{bmatrix} \sigma_{11} \\ \sigma_{22} \\ \sigma_{33} \\ \sigma_{23} \\ \sigma_{13} \\ \sigma_{12} \end{bmatrix} = \frac{E}{(1+\nu)(1-2\nu)} \begin{bmatrix} 1-\nu & \nu & \nu & 0 & 0 & 0 \\ \nu & 1-\nu & \nu & 0 & 0 & 0 \\ \nu & \nu & 1-\nu & 0 & 0 & 0 \\ 0 & 0 & 0 & \frac{(1-2\nu)}{2} & 0 & 0 \\ 0 & 0 & 0 & 0 & \frac{(1-2\nu)}{2} & 0 \\ 0 & 0 & 0 & 0 & 0 & \frac{(1-2\nu)}{2} \end{bmatrix} \begin{bmatrix} \epsilon_{11} \\ \epsilon_{22} \\ \epsilon_{33} \\ 2\epsilon_{23} \\ 2\epsilon_{13} \\ 2\epsilon_{12} \end{bmatrix} - \frac{E\alpha\Delta T}{1-2\nu} \begin{bmatrix} 1 \\ 1 \\ 1 \\ 0 \\ 0 \\ 0 \end{bmatrix}
$$
$$(4.9)$$

where E represent Young's modulus, ν Poisson's ratio, α the coefficient of thermal expansion and ΔT is the increase in the temperature [30]. The Bulk modulus, K, can also be obtained from Young's modulus and Poisson's ratio through the following relation

$$ K = \frac{E}{3(1-2\nu)}, \tag{4.10} $$

and gives a measure of a body's resistance to changes in its volume. To implement the force exerted on the PDMS layer, a "Body load" was included in the COMSOL model. The r- and z-components of the load was set to equal

$$ r = -3 \cdot solid.K \cdot material.alpha\_iso \cdot Tr \tag{4.11} $$
$$ z = -3 \cdot solid.K \cdot material.alpha\_iso \cdot Tz, \tag{4.12} $$

where the Bulk modulus and thermal expansion coefficient were defined as before. Additionally, Tr and Tz denoted the derivatives of the temperature in the r- and z-directions, respectively. The $"3 \cdot K"$ expression resulted in the expression of $\frac{E}{1-2\nu}$, from equation 4.9. It was chosen instead of obtaining the values for Poisson's ratio and Young's modulus separately for the material.

4.3.2 Laser intensity

To implement the laser intensity in the model, a *Dirichlet boundary condition* was implemented on the lower half of the PDMS layer, as shown in figure 4.1. This would simulate a laser beam originating from underneath the setup, focused at the PDMS layer. The boundary condition consisted of the equation $In = r$, where In was defined as the intensity and was set equal to

$$r = I0 \cdot Ldis(r) \cdot ft(t) \tag{4.13}$$

at the chosen boundary. I0 represented the intensity of the laser, which was given the value 10^6 W/m^2. Ldis(r) represented the function for the Gaussian beam shape of the laser, and ft(t) denoted the Gaussian pulse function mentioned in section 4.3.

To compute the temperature profile, another Dirichlet boundary condition was applied to the boundaries of the PDMS layer, as shown in figure 4.1. The boundary condition set the temperature on the selected edges equal to the reference temperature, Tref. Which ensured that the small increase in temperature in the PDMS layer did not cause a change in temperature in the surrounding elements.

4.3.3 Ultrasonic transducer

To be able to receive the information from the US waves emitted by the PDMS layer, an ultrasonic transducer was implemented in the COMSOL model. The transducer was modeled with two components; a piezoelectric polymer and a backing material. For the piezoelectric component, a thin film of Polyvinylidene Fluoride (PVDF) was implemented. A layer of water functioned as the backing material. In addition, electrodes were implemented on the lower part of the PVDF layer, and partially on the upper boundary. The length of the upper electrode defined the aperture width of the transducer. The remaining boundaries surrounding the PVDF layer were set as Ground. Table 4.1 includes the global parameters defining the dimensions of the transducer. Since the transducer was used only to receive signals and not transmit them, the charge on the electrodes were set to zero. The remaining boundaries around the PVDF film were chosen as ground.
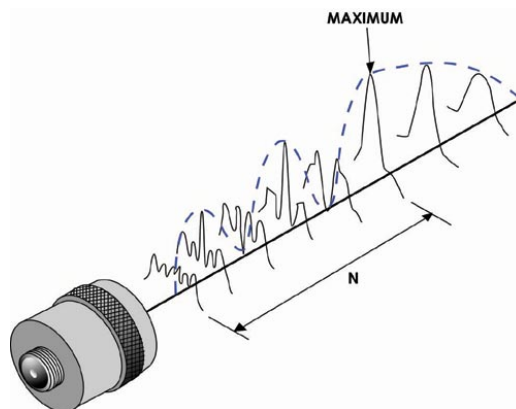
Figure 4.3: Illustration of signal behavior in the near and far field of an ultrasonic transducer. The signal is strongest in the transition between the fields. Image from [31].

Since the transducer is the most sensitive in the region that marks the transition between the near- and far field, it was preferable that the source of the US waves was situated there. Figure 4.3 illustrates the wave behaviour in the near- and far field of a transducer; the signal is strongest and most well behaved at the end of the near field [31]. Further into the far field, the strength of the signal decreases with distance from the transducer. To calculate the aperture width needed to achieve the ideal near-field length, the near field formula from [32] was applied:

$$N = \frac{D^2 F}{4V} \tag{4.14}$$

$$D^2 = \frac{N \cdot 4V}{F}, \tag{4.15}$$

where N is the near field length, D is the aperture diameter, F is the frequency of the transducer and V is the sound speed in the material. Deciding on an estimate for the transducer frequency F, the signal and frequency spectrum for an aperture diameter of 200 μm was plotted. Figure 4.4

50

includes both the signal and its frequency spectrum. The frequency corresponding to the maximum value of the spectrum, here 16 MHz, was used as an estimate for F. Furthermore, the PVDF film had a thickness of $p_{tran} = 24\mu$m. For the transition between the fields to be placed on the upper boundary of the PDMS layer, where the acoustic wave originated from, the near field length should be

$$N = p\_tran + T\_water \tag{4.16}$$

$$= 24\mu m + 400\mu m \tag{4.17}$$

$$= 424\mu m. \tag{4.18}$$

Inserting the values into equation 4.15, an estimate for the aperture width was found to be

$$D^2 = \frac{424\mu m \cdot 4 \cdot 1500m/s}{16MHz} \tag{4.19}$$

$$D^2 = 15.90\mu m \tag{4.20}$$

$$D \approx 400\mu m. \tag{4.21}$$

Thus, the aperture width was set to 400 μm. Figure 4.5 shows the model after the transducer was implemented. The width of the sample area was increased to 450 μm, to better convey the transducer configuration. Note that the boundary conditions were identical to the model in Figure 4.1, and an additional spherical reflection boundary were implemented around the water backing layer.
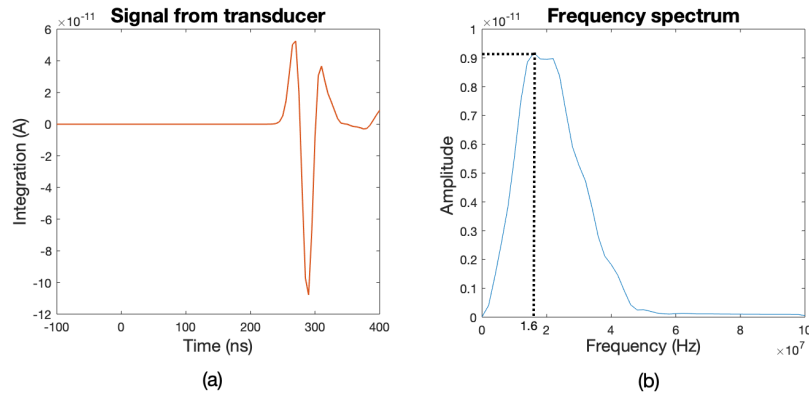
Figure 4.4: (a) A signal received by the transducer in the COMSOL model, and (b) the frequency spectrum corresponding to the signal. The spectrum had a peak frequency at 16 MHz, which was used as an estimate for the transducer frequency F.
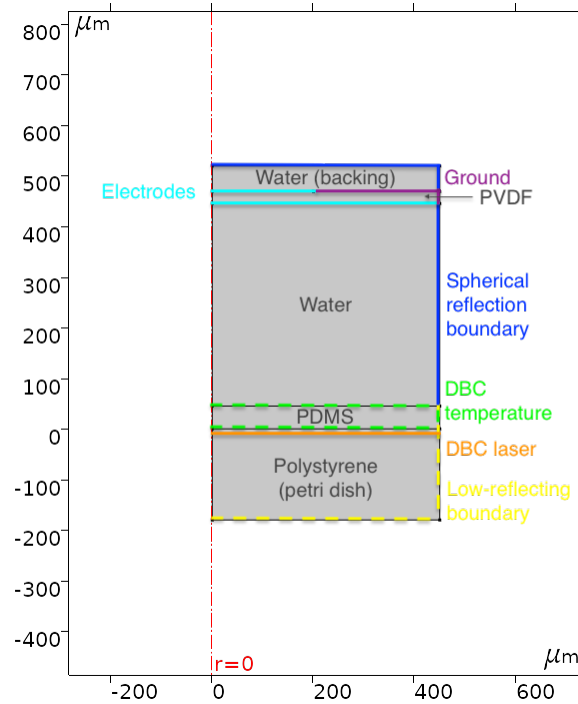
Figure 4.5: The COMSOL model with the ultrasonic transducer. The transducer consisted of a thin film of the piezoelectric polymer PVDF, and water as the backing material. The placement of the electrodes are marked with turquoise lines. The boundary conditions were defined as in Figure 4.3, but with an additional spherical reflection boundary around the backing layer as well as ground on the remaining boundaries of the PVDF film. DBC = Dirichlet boundary condition.

Chapter 5

Results

5.1 Numerical Investigation

This section is dedicated to results obtained from the model implemented in COMSOL Multiphysics. First of all, the physical parameters and their impact on the simulation were analysed to ensure that the model was suitable as an estimate for real life events. In addition, the frequency distribution of the obtained signals were analyzed to determine how and to what degree the physical parameters affected it.

5.1.1 Physics Study

To ensure that the physics represented in the COMSOL simulation were correct, it would be wise to change some of the parameters and observe if the model behaved as expected. These tests were executed for the first model, discussed in Section 4.3, which did not include the transducer. The model was simulated for two different values of the layer absorption coefficient, the layer thickness and the laser beam width. The resulting acoustic pressure fields were compared to each other at an arbitrary time of $t = 250$ ns. At this point in time, both the acoustic wave and the reflected wave from the bottom of the petri dish were visible in the acoustic pressure field. A weak wave reflected from the right side of the water layer was observable at this time step as well. Table 5.1 contains the two separate values which was applied for the layer absorption coefficient, layer thickness and laser beam width.

Table 5.1: Two different values used for each parameter to simulate the effects occurring by increasing/decreasing their values.

Parameter	Value 1	Value 2
mu0	$1/20\ \mu m^{-1}$	$1/40\ \mu m^{-1}$
si0	$5\ \mu$m	$10\ \mu$m
T_pdms	$15\ \mu$m	$30\ \mu$m

First, the layer absorption coefficient was altered. When the absorption coefficient was increased, a larger portion of the laser light would be absorbed by the material. Thus, there would be an increase in temperature causing the acoustic pressure to increase as well. To determine if the COMSOL model behaved as expected, it was executed for the two values; $1/40\ \mu m^{-1}$ and $1/20\ \mu m^{-1}$. Figure 5.1 includes the acoustic pressure field for both values, at $t = 250$ ns. For the larger absorption coefficient, there was an increase in the acoustic pressure, as expected. For further testing of the PDMS thickness and the laser beam width, the absorption coefficient was set constant to $1/40$ μm^{-1}.

Then, the thickness of the PDMS layer was changed. Results were obtained for two thicknesses, 15 μm and 30 μm respectively. Figure 5.2 illustrates the acoustic pressure field for both thicknesses. When the thickness was doubled, there was a slight increase in the acoustic pressure of the wave. As expected, a thicker layer absorbs more of the laser light and thus emits US waves with larger acoustic pressure. The PDMS thickness was then set to equal 30 μm for the last coefficient.

At last, the width of the laser beam was modified. As before, two different values were tested; widths of 5 μm and 10 μm. Figure 5.3 includes the acoustic pressure obtained for both beam widths. Note, that the acoustic pressure was noticeably larger when the beam width was doubled. The wider beam caused a larger area of the PDMS layer to experience heating, thus producing stronger acoustic waves, as expected.

In addition to the acoustic pressure fields, the intensity and temperature profiles for the PDMS layer were plotted. Figure 5.4 includes the plots for both beam widths, note that the window was zoomed in on the area of interest. The temperature profile was shown as the difference from the reference temperature, Tref.

Notice that the width of the area that experienced an increase in intensity, was approximately doubled when the beam width was doubled. Thus, the area having an increase in temperature also expanded, as seen in the temperature profiles. Consequently, the amplitude of the acoustic wave was significantly larger for the wider laser beam. Observe as well that the increases in intensity and temperature were highest at the bottom of the PDMS layer, and decreased with the distance

travelled through the layer. Furthermore, recognize from the temperature profiles that the boundary condition causing the temperature on the edges to equal Tref, was functioning as intended. The ultrasonic waves propagating through the water were in the shape of surface waves.

(a) Absorption coefficient $1/40$ μm^{-1}.

(b) Absorption coefficient $1/20$ μm^{-1}.
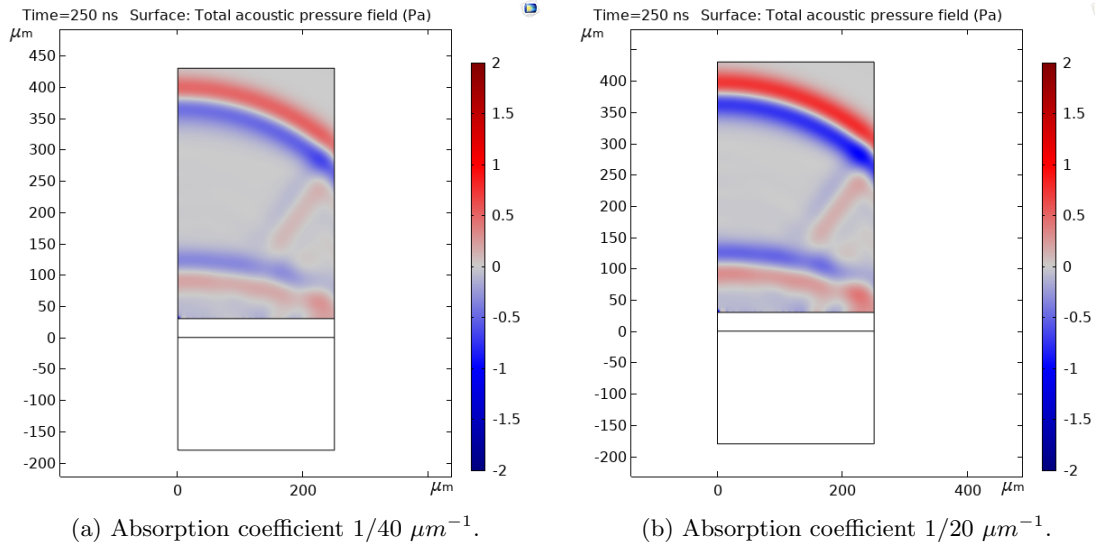
Figure 5.1: The acoustic pressure fields for two different values of the absorption coefficient; $1/40$ μm^{-1} and $1/20$ μm^{-1}. The pressure increased when the absorption coefficient was increased, in accordance with theory.

(a) Thickness of PDMS layer set to 15 μm.

(b) Thickness of PDMS layer set to 30 μm.
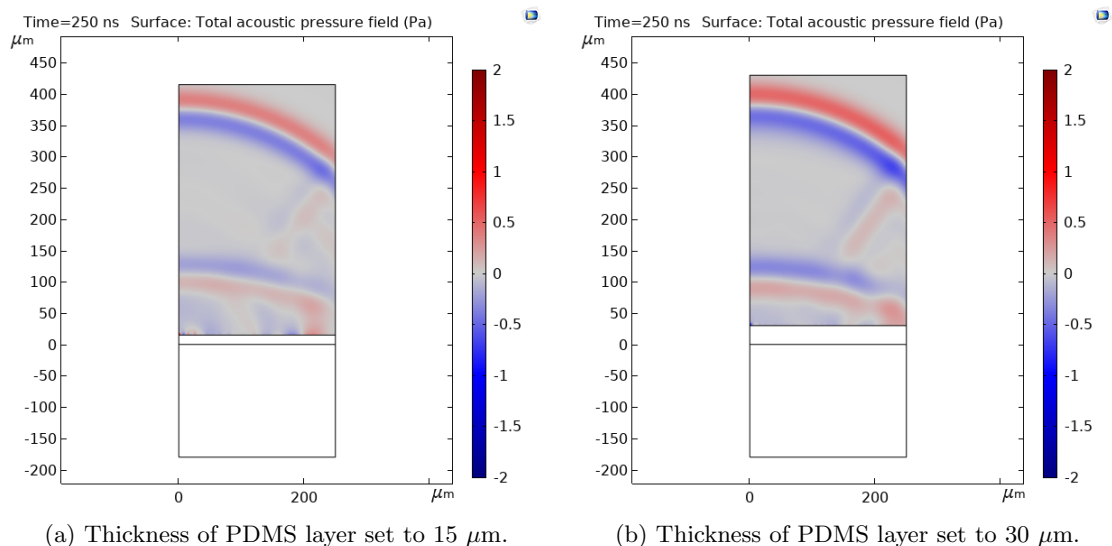
Figure 5.2: The acoustic pressure fields for two different thicknesses of the PDMS layer; 15 μm and 30 μm, namely. The pressure increased when the thickness of the layer was increased, as expected.

(a) Laser beam width equal to 5 μm.

(b) Laser beam width equal to 10 μm.
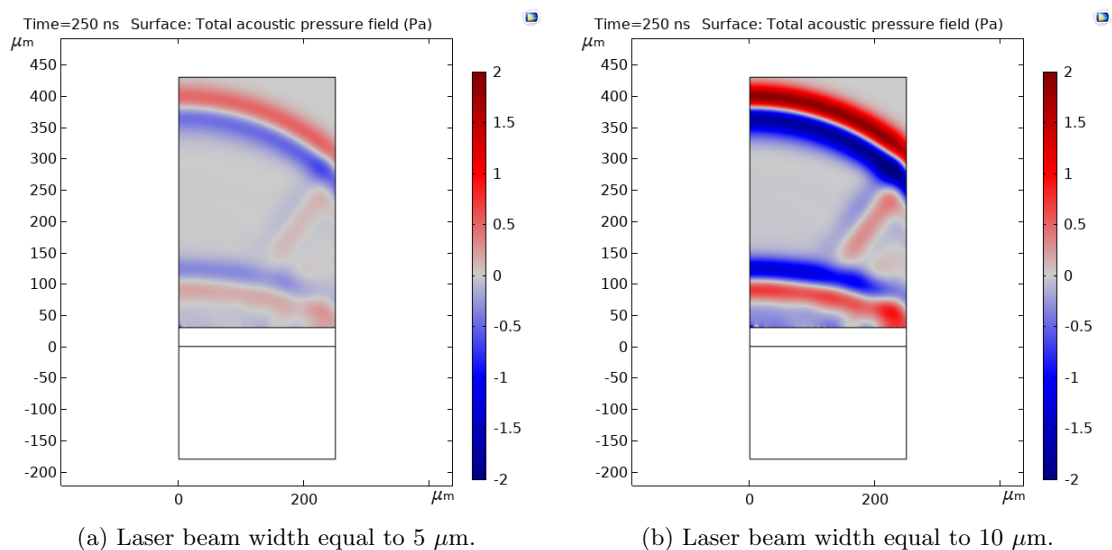
Figure 5.3: The acoustic pressure fields for two different laser beam widths; 5 μm and 10 μm, respectively. The pressure increased when the beam width was increased, in accordance with theory.

(a) Laser beam width of 5 μm.

(b) Laser beam width of 10 μm.

(c) Laser beam width of 5 μm.

(d) Laser beam width of 10 μm.
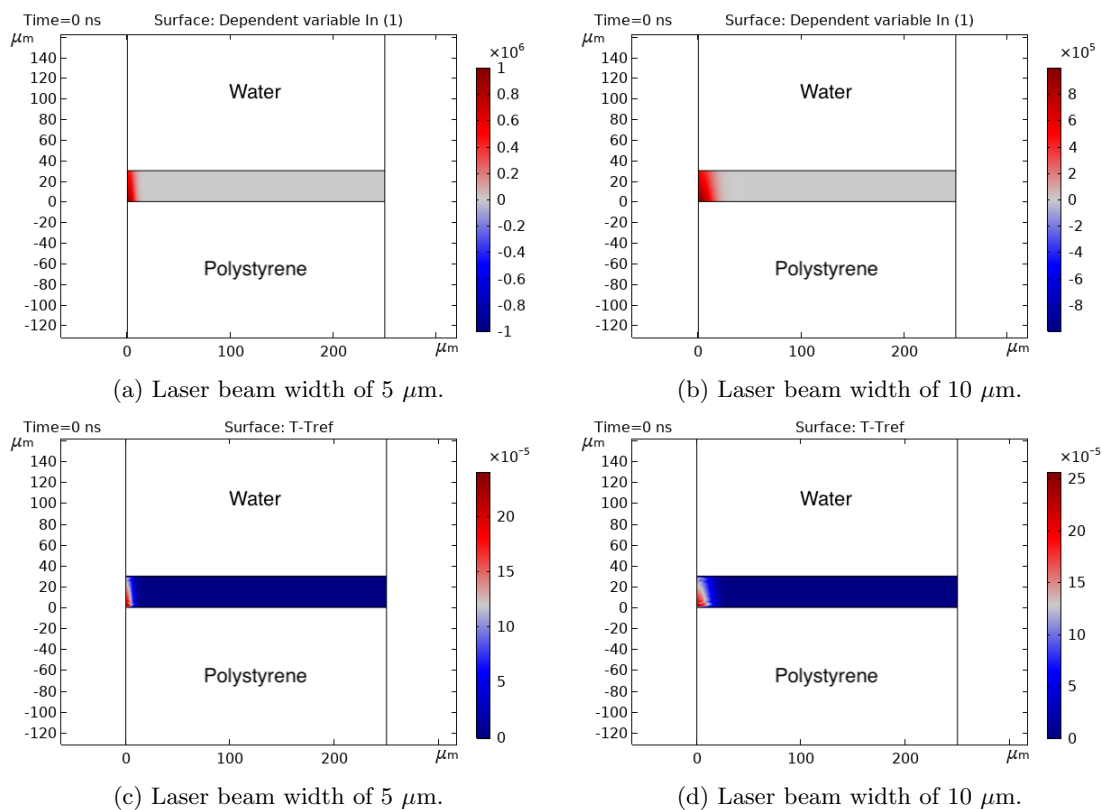
Figure 5.4: Top row: Intensity profile in the PDMS layer for a laser beam width of (a) 5 μm and (b) 10 μm. The intensity range was approximately doubled for the 10 μm beam width. Bottom row: Temperature profile, with reference to Tref, in the PDMS layer for a laser beam width of (c) 5 μm and (d) 10 μm. When the beam width was increased, a larger area of the PDMS layer experienced an increase in temperature.

5.1.2 Frequency Distribution

To determine how the different factors impact the frequency distribution of the acoustic signal, the frequency spectra of the signal were analysed. In total, four different values of the thickness of the PDMS layer were tested for four values of the absorption coefficient, resulting in 16 different combinations. The center frequency f_c, full-width at half-maximum (FWHM) and the percent bandwidth %BW were found from the frequency spectrum. The FWHM in wavelength was calculated from equation 2.1, and %BW was found from equation 2.2.

Figure 5.6 includes the initial acoustic wave of one of the received signals, corresponding to a PDMS thickness of 35 μm and an absorption coefficient of 1/30 μm^{-1}. The frequency spectrum of the signal is represented in Figure 5.7. The upper and lower frequencies were identified in this figure as well. The normalized values were plotted as functions of the absorption coefficient in separate plots for the PDMS thicknesses, and are included in Figure 5.5. The trend was similar for all thicknesses; the percent bandwidth and FWHM increased when the absorption coefficient decreased, while the center frequency decreased. When the PDMS thickness was increased, all the parameters experienced more rapid variations between the different absorption coefficients.

Table 5.2: Resulting values for center frequency (f_c), full-width half-maximum (Δl) and percent bandwidth (%BW). Calculated for 16 different combinations of film thickness (T_pdms) and absorption coefficient (mu0).

T_pdms [μm]	mu0 [μm^{-1}]	f_c [MHz]	Δl [μm]	%BW [%]
15	1/10	13.97	110.9	103.38
	1/20	13.92	111.4	103.42
	1/30	13.90	111.6	103.47
	1/40	13.89	111.8	103.53
25	1/10	13.89	112.1	103.90
	1/20	13.67	114.6	104.51
	1/30	13.60	115.4	104.67
	1/40	13.56	115.7	104.70
35	1/10	13.90	113.2	104.92
	1/20	13.40	119.3	106.68
	1/30	13.20	121.9	107.40
	1/40	13.20	122.0	107.40
45	1/10	14.00	113.1	105.56
	1/20	13.21	123.0	108.43
	1/30	12.82	127.1	108.70
	1/40	12.65	129.1	108.98
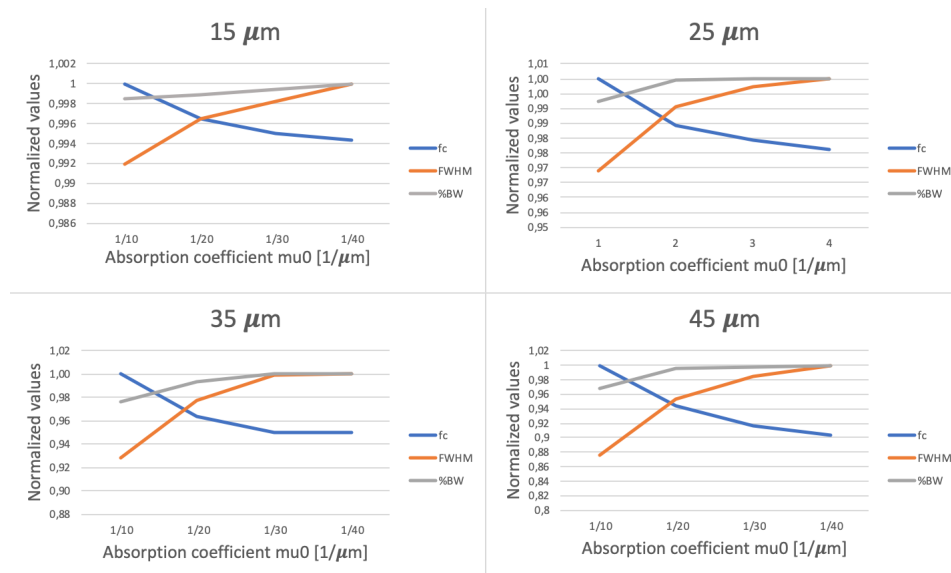
Figure 5.5: Center frequency (fc), full-width at half-maximum (FWHM) and percent bandwidth (%BW) as functions of absorption coefficient (mu0), for four different film thicknesses. The values were normalized.
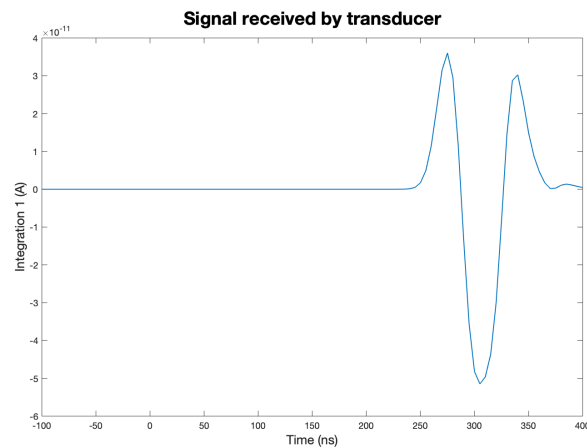
Figure 5.6: Signal resulting from integrating over the transducer in the COMSOL model. It corresponds to a PDMS thickness of 35 μm and an absorption coefficient of $1/30$ μm^{-1}. This plot only included the incident wave.
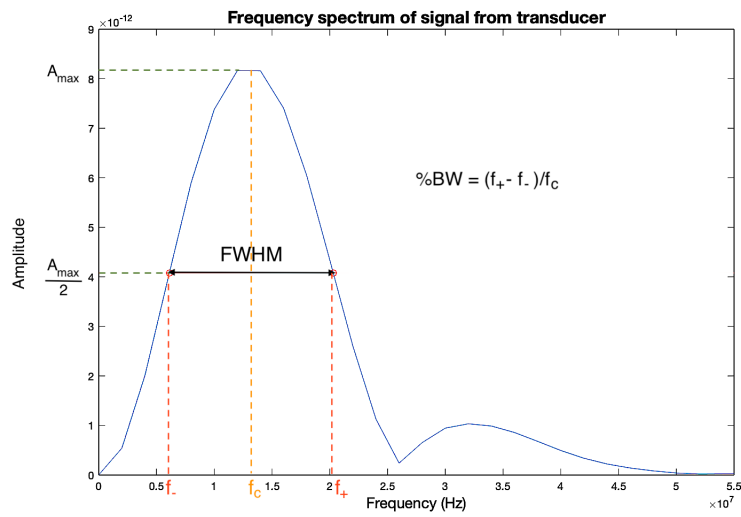
Figure 5.7: Frequency spectrum of the incident wave of the signal corresponding to a 35 μm thick layer of PDMS, and an absorption coefficient of $1/30$ μm^{-1}. The bandwidth was found from the difference between the upper and lower frequencies, f_+ and f_-.

5.2 Experimental Investigation

For the experiments, two PAFs with different amounts of toner particles were investigated. The main interest of these investigations was to show how well the toner particles absorbed light. Additionally, a central part was to compare the results obtained in this section with the simulated results obtained in Section 5.1.

5.2.1 Data Recording

The experiment was set up as described in Section 3.1. Two samples with different concentrations of toner particles to PDMS were imaged. Sample 1 had a concentration of 0.5 grams toner particles, while sample 2 had 1 gram toner particles to the same amount of PDMS solution. Both samples were spin coated at 4000 RPM. Figure 5.8 includes the optical images of the samples. The 1 mm by 1 mm areas scanned for the photoacoustic image are indicated by the dotted lines. For referencing, the images were taken including air bubbles that arose while filling the petri dishes with water. In addition, the optical image of sample 1 included a line which was more saturated with particles than the surrounding area. The origin of this line was uncertain. It was also possible to observe the difference in amount of toner particles from the optical images, as sample 2 had a denser, more homogeneous distribution of particles.

To plot the images, the largest intensities were found for each pixel and multiplied by a scaling factor to obtain a set of 16 bit integers. Then, the values were converted to a dB scale (20log) and plotted. The images were 200 by 200 pixels large, meaning that one pixel corresponded to $1/200 = 0.005$ mm or 5 μm. The photoacoustic images obtained for the scan areas in their entirety are included in Figure 5.9. The yellow areas denoted the toner particles in the coating. Due to US waves not propagating well through air, the intensity of the acoustic waves emitted from the bubbles were lower than for the surrounding areas. Note as well that the saturated line in sample 1 emitted higher intensity waves, due to it absorbing more light. In the remaining areas, sample 2 had an overall higher intensity compared to sample 1. While sample 2 had an even distribution of particles, sample 1 had larger areas in between where the intensity was low.

An arbitrary pixel in the photoacoustic image for sample 2 contained the intensity profile plotted in Figure 5.10. The window has been scaled to show the acoustic wave emitted from the coating after illuminating it with the laser light, hereafter referred to as the incident wave. In addition, a second wave hit the transducer some time after the first one. The delay between these waves were approximately 175 ns, measured between their maximas. If an acoustic wave were to be reflected

from the bottom of the 180 μm thick petri dish, and it is known that the thickness of the PDMS coating was around 13 μm it would take

$$t = \frac{2 \cdot 13}{1119} + \frac{2 \cdot 180}{2350} \approx 176 \text{ ns} \tag{5.1}$$

to travel this distance. The sound speeds were gathered from Table 3.1. Hence, the second acoustic wave reaching the transducer was the wave reflected from the bottom of the petri dish. From equation 2.3 and the acoustic impedances listed in Table 3.1, the reflection coefficient of this wave was calculated. Due to the specifications of the petri dish only revealing that the dish consisted of some polymer, the values for polystyrene were used as substitutes. First, the reflection between water and polystyrene was found to decide how much of the energy from the incident wave reached the bottom of the petri dish. This gave a reflection coefficient of

$$R_{water,poly} = \left(\frac{2.52 - 1.48}{2.52 + 1.48}\right)^2 = 0.067, \tag{5.2}$$

which means that the transmission coefficient was

$$T_{water,poly} = 1 - 0.054 = 0.932. \tag{5.3}$$

Thus, $\approx$7 % of the incident wave energy was reflected off the boundary and $\approx$93 % of the energy was transmitted to the bottom of the petri dish. The reflection coefficient between polystyrene and air was calculated to

$$R_{poly,air} = \left(\frac{0.000401 - 2.52}{0.000401 + 2.52}\right)^2 = 0.999. \tag{5.4}$$

99 % of the energy transmitted to the bottom of the petri dish was reflected off of it. To obtain this amount as the percentage of the incident wave energy, the reflection coefficient had to be multiplied by the transmission coefficient found previously;

$$R_{incident} = T_{water,poly} \cdot R_{poly,air} = 0.932 \cdot 0.999 = 0.931. \tag{5.5}$$

Approximately 93 % of the energy of the incident wave was reflected from the bottom of the petri

dish. While travelling towards the transducer again, ≈7 % of the energy would be reflected off the boundary between the petri dish and water. Hence, approximately 88 % of the energy of the incident wave was transmitted towards the transducer from the bottom of the petri dish. At the same time, only 7 % of the energy was reflected from the top of the petri dish. This explains why the reflected wave had a peak intensity that was larger than the peak intensity of the incident wave in Figure 5.10.
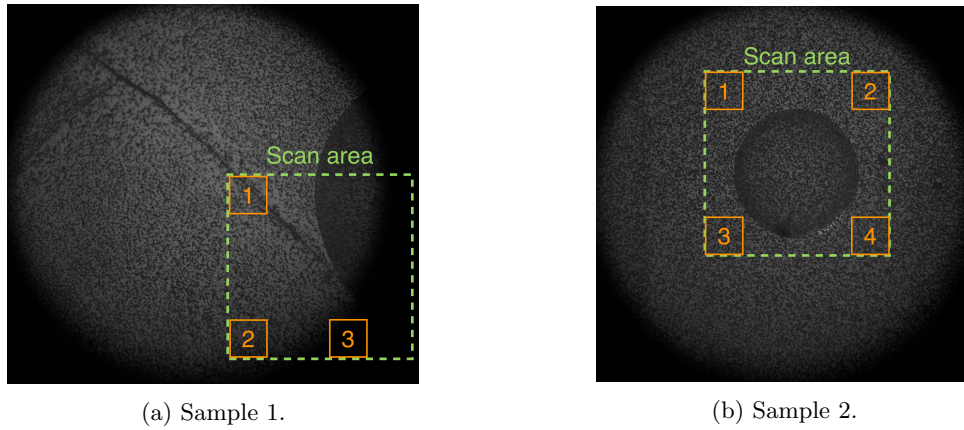
(a) Sample 1.   (b) Sample 2.

Figure 5.8: Optical images of the scan area for the two samples, marked by a dotted rectangle. The scan area is 1mm by 1 mm. The numbered rectangles are 40 by 40 pixels, or 0.2 mm by 0.2 mm.
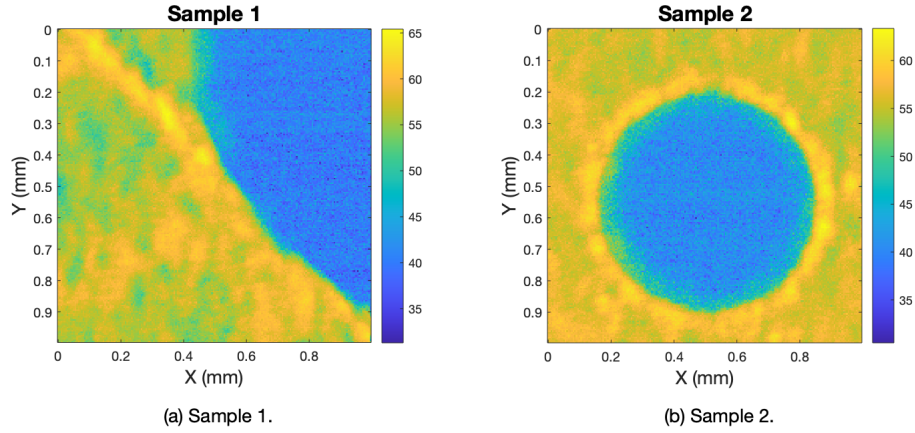
(a) Sample 1.   (b) Sample 2.

Figure 5.9: Photoacoustic images of (a) sample 1 and (b) sample 2, plotted on a dB scale. The blue area defines the air bubbles included in the images, they had a lower intensity due to the properties of US waves in air.
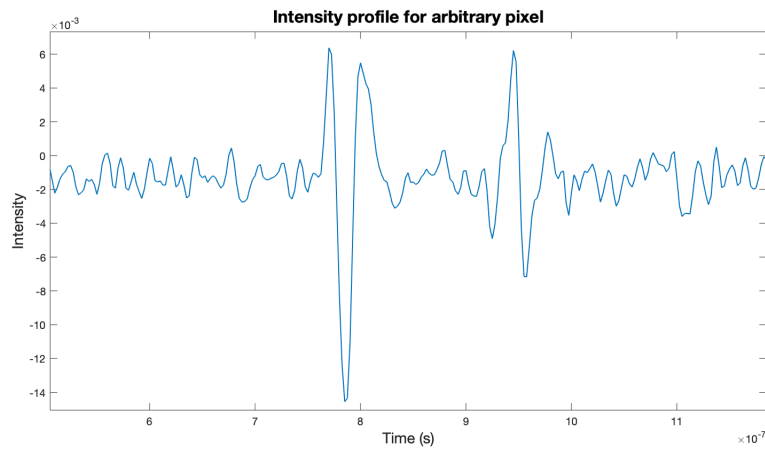
Figure 5.10: Intensity profile for an arbitrary pixel in the photoacoustic image produced for sample 2. The second acoustic wave was received 175 ns after the incident acoustic wave.

5.2.2   Time Domain Analysis

Calculating Tilt of Samples

After placing the petri dish in the sample holder on the stage, a spirit level was used to level the sample horizontally. Regardless, it was presumed that some amount of tilt would still be present. To calculate the tilting, the intensity profile as function of time for each corner of the scan area was plotted. The phase shift between the time series were then found by cross correlation in MATLAB. The numbered squares in Figure 5.8 indicates the smaller areas used for calculations. The size of each square was 40 by 40 pixels (or 0.2 mm by 0.2 mm), and the intensity profile was plotted for the center pixel of each square. Due to the unfortunate placement of the air bubble in the photoacoustic scan of sample 1, only three of its corners were suited for comparison.

Figure 5.11 includes the sections of the photoacoustic image used to calculate tilt for sample 1. The intensity profiles for each center pixel are plotted in Figure 5.13, along with a zoomed in section covering the received main acoustic wave. Note that the wave from area 1 reaches the transducer faster than areas 2 and 3, meaning that area 1 is more elevated. Area 3 is more elevated than area 2, thus the sample was tilted towards area 2. Setting area 1 as the reference point, the time delay and phase shift could be found from cross correlation in MATLAB. Table 5.3 includes the values for areas 2 and 3 of sample 1. As observed from the plot, the US wave emitted from area 2 was more delayed than from area 3. Using that the sound velocity in water is 1490 m/s, the height difference between area 1 and area 2 in length could be calculated to

$$dl = 1490\text{m/s} * 12.5 \cdot 10^{-9}\text{s} = 18.75\mu m. \tag{5.6}$$

The four areas used to calculate tilt for sample 2 are included in Figure 5.12. The intensity profiles corresponding to the center pixel of each area are plotted in Figure 5.14. As for sample 1, the time delay and phase shift was calculated and included in Table 5.4. By analyzing the values and the plot it was observed that the sample tilted towards the bottom right corner, where area 4 was located. As for the 1st sample, the height difference was found between area 1 and area 4;

$$dl = 1490\text{m/s} * 10 \cdot 10^{-9}\text{s} = 14.9\mu m. \tag{5.7}$$

Thus, sample 1 experienced more tilt than sample 2. Moreover, the samples did not tilt in the same directions: by observing the optical images in Figure 5.8 with respect to area 1, sample 1 tilted

towards area 2 while sample 2 tilted towards area 4.

Table 5.3: Time delay and phase shift calculated with respect to area 1 of sample 1.

Area	Time delay (ns)	Phase shift (deg)
2	12.5	0.045
3	10	0.036

Table 5.4: Time delay and phase shift calculated with respect to area 1 of sample 2.

Area	Time delay (ns)	Phase shift (deg)
2	2.5	0.009
3	7.5	0.027
4	10	0.036
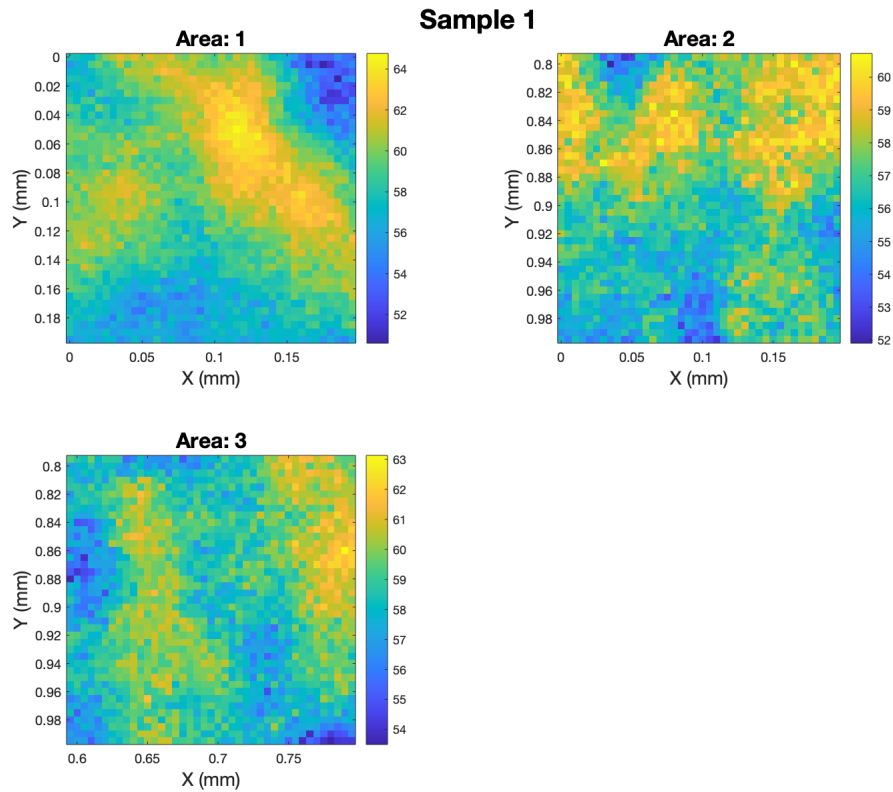
Figure 5.11: The 40 by 40 pixel areas used to calculate the tilt of sample 1. Due to the placement of the air bubble in the photoacoustic image, only three areas were suited for calculations.
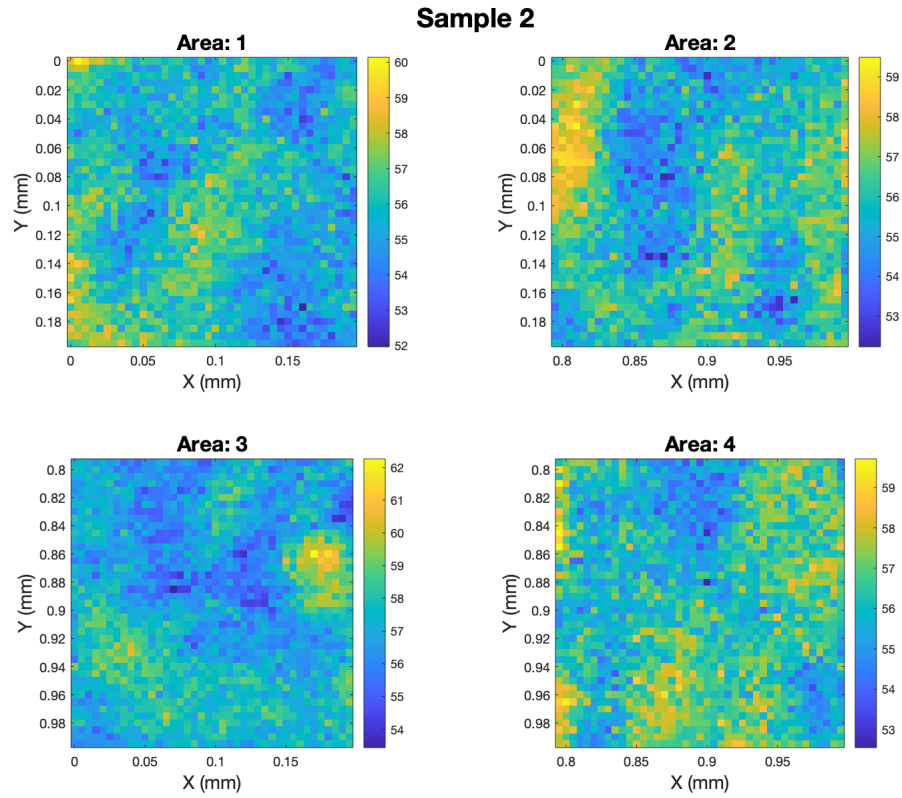
Figure 5.12: The 40 by 40 pixel areas used to calculate the tilt of sample 2, one for each corner of the photoacoustic image.
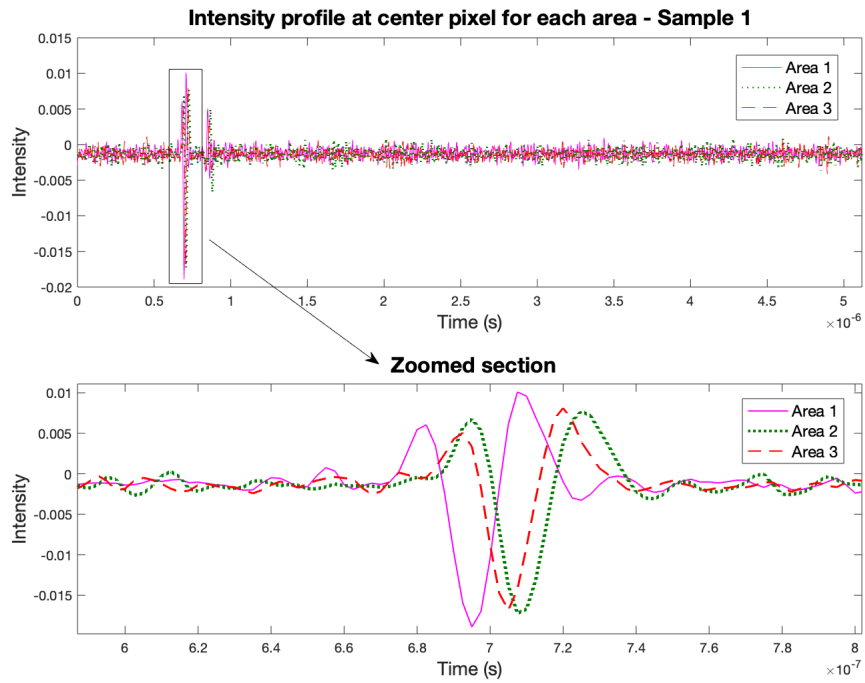
Figure 5.13: The intensity profile at the center pixel of each area in Figure 5.11, plotted along with a zoomed in selection of the incident acoustic waves.
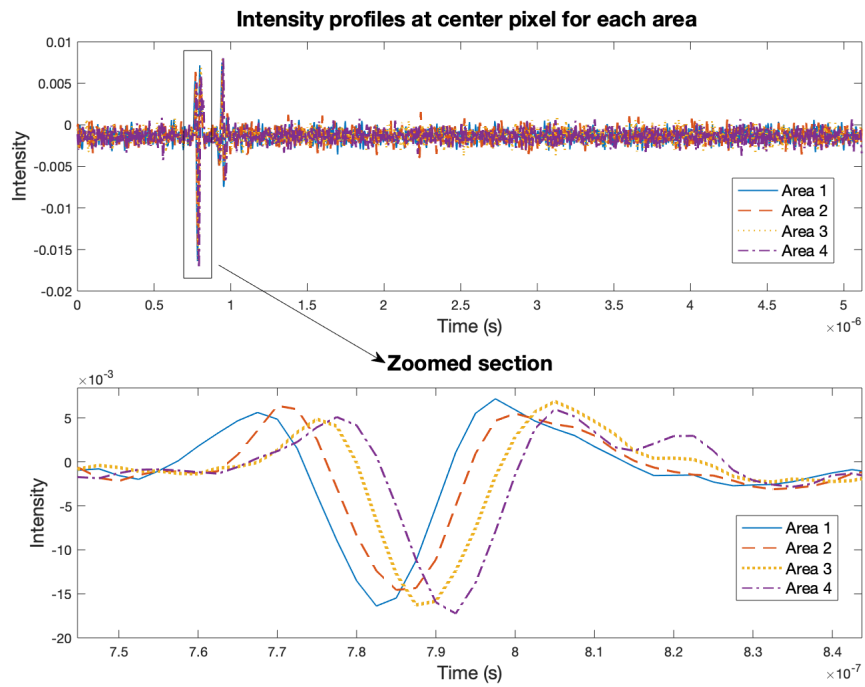
Figure 5.14: The intensity profile at the center pixel for each of the four areas in Figure 5.12. As for sample 1, a zoomed in selection of the incident acoustic waves were included.

Mean Intensity and Standard Deviation

To calculate the mean intensity of the samples, an area with approximate uniform distribution of toner particles was chosen. This means that the air bubbles and the highly saturated line in sample 1 were avoided. As before, the areas chosen for calculations were 40 by 40 pixels large. By calculating the mean value for each time-step for all the pixels, the mean intensity profile was obtained. Figure 5.15 includes the mean intensity plot for both sample 1 and 2. The mean maximum intensity of the US waves emitted from sample 1 was $0.0051 \cdot 10^{-3}$, while sample 2 had a maximum intensity of $0.0056 \cdot 10^{-3}$. It should also be noted that the mean acoustic signal from sample 2 was delayed with respect to sample 1 by 77.5 ns. The time delay relates to a spatial offset of 116.2 μm between the samples.

In addition, the standard deviation for the two 40 by 40 pixel sections were calculated and plotted in Figure 5.16. Both samples had a maximum standard deviation of $0.0026 \cdot 10^{-3}$ from the mean intensity of the area.
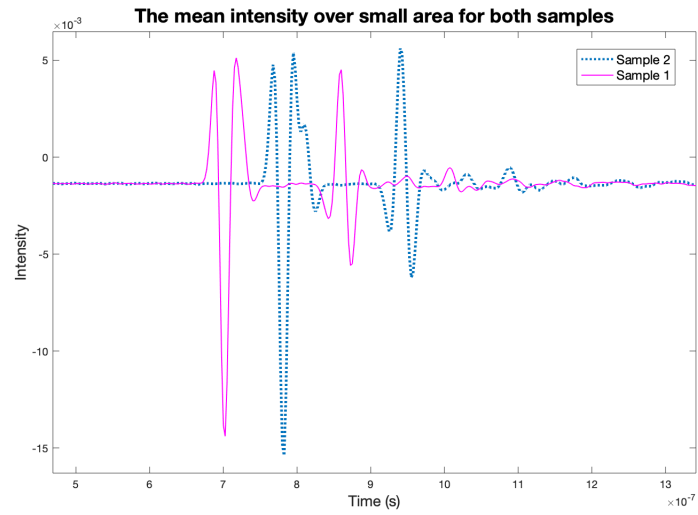
Figure 5.15: Mean intensity profiles over a 40 by 40 pixel area with an approximate uniform distribution of toner particles, for both samples. Sample 2 had a slightly higher mean maximum intensity for the incident acoustic wave.
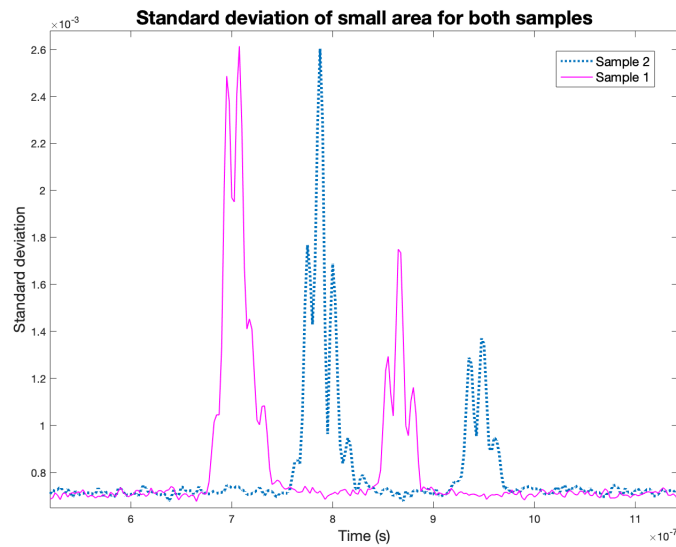
Figure 5.16: The standard deviation for the 40 by 40 pixel selections for both samples. Both areas had a maximum deviation of 0.0026.

71

Comparison Between Experimental and Numerical Data

To compare the data from the experiment with the simulated data, they were plotted together. The experimental and simulated waves did not have the same scale in neither the x- nor y-direction, therefore the signals had to be normalized and time shifted before they could be plotted together. Figure 5.17 shows the mean intensity profile for both areas of the samples, compared to the simulated signal from the model. For the model, a PDMS thickness of 15 μm, a laser beam width of 5 μm and an absorption coefficient of $1/30$ μm^{-1} were used. Observe that the waveform of the experimental data had a high resemblance to the waveform of the simulated signal. The most notable difference occured in the peak-to-peak amplitude of the incident acoustic wave, where the simulated signal had a lower value.
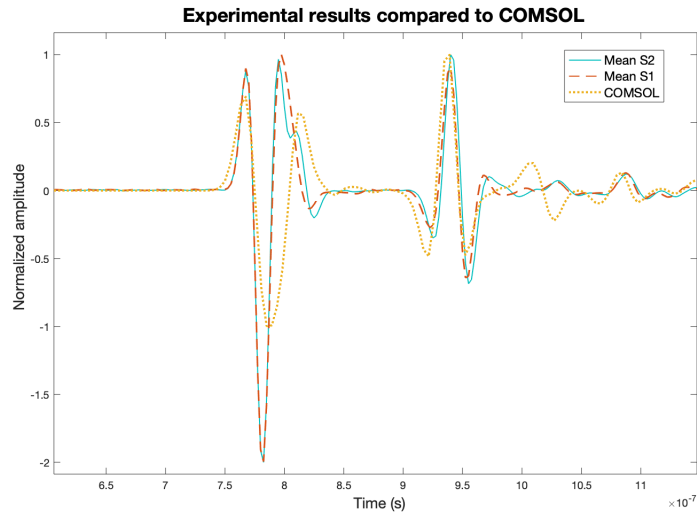
Figure 5.17: Mean intensities for sample 1 (S1) and sample 2 (S2), compared to the acoustic wave simulated in the COMSOL model.

5.2.3 Frequency Domain Analysis

Frequency Spectrum

To compute the frequency spectra, the same 40 by 40 pixel areas used for finding the mean intensity and standard deviation were utilized. The frequency spectrum was plotted for the mean intensity profile and for the center pixel of the selection, for both samples. Plots are included in Figures 5.18 and 5.19 for sample 1 and sample 2, respectively. The frequencies corresponding to the maximum values of the spectra are listed in Table 5.5. The frequency spectrum for the mean intensity had a lower peak frequency compared to the frequency spectrum of the intensity in the center pixel, for both samples. From Appendix B, the frequency response of the PVDF transducer had a peak frequency of 35.40 MHz. The peak frequencies for the intensity in the center pixels were close to this value, at 34.4 MHz and 34.8 MHz. For the mean intensity spectra, the peak frequencies were shifted downwards compared to the UT peak frequency, and had values of 22.1 MHz and 28.9 MHz. The higher peak frequencies for the center pixels could be due to its higher noise level of the non-averaged signal.

Furthermore, the frequency spectra of the mean intensities were compared to the frequency spectrum of the simulated signal from Figure 5.17. The frequency spectra were normalized and plotted together in Figure 5.20. The waveform of the simulated spectrum was similar to the experimental waveforms, but shifted to the left. The frequency spectrum for the simulated signal had a peak frequency of 15 MHz.

Table 5.5: Peak frequencies for the frequency spectra of the mean intensity and the center pixel intensity, in sample 1 and sample 2.

Sample	Mean (MHz)	Center (MHz)
1	22.1	34.4
2	28.9	34.8

Figure 5.18: Frequency spectra of the mean intensity profile and the intensity profile of the center pixel, for the same 40 by 40 pixel area of sample 1.

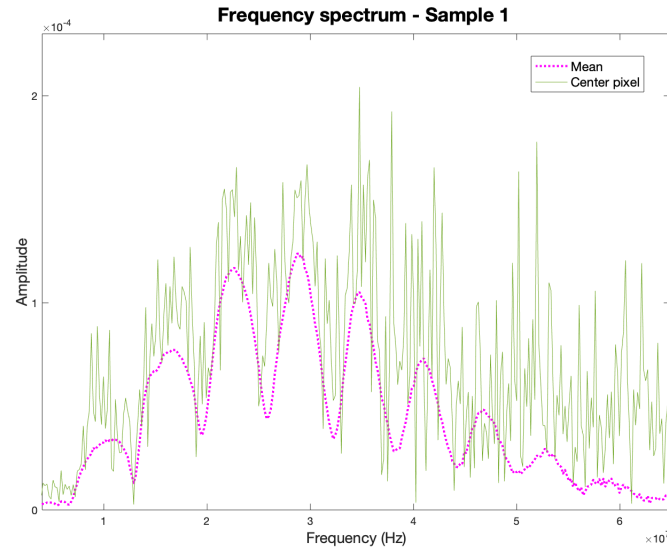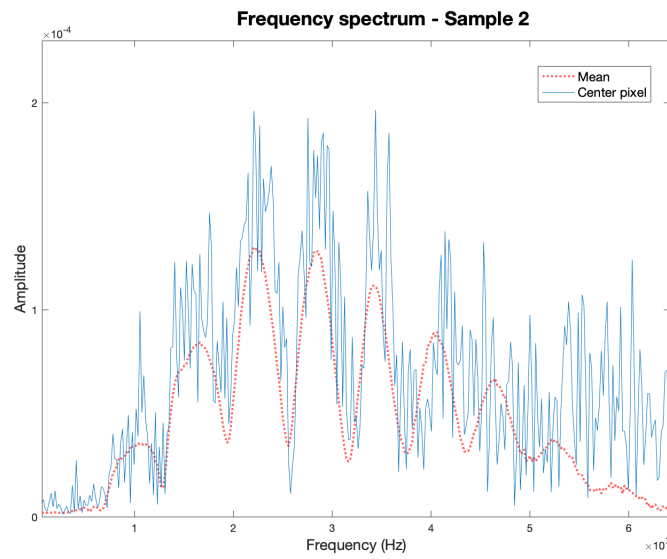Figure 5.19: The frequency spectra for the mean intensity and the intensity profile of the center pixel, for a 40 by 40 pixel area of sample 2.
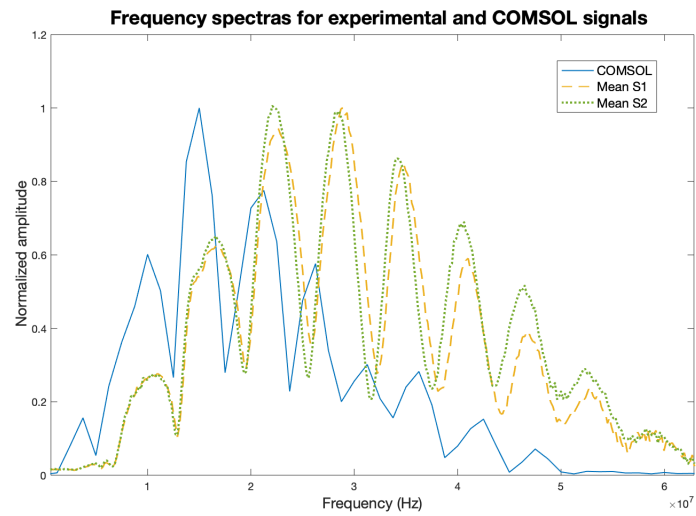
Figure 5.20: Comparison of frequency spectra between the experimental results and the simulated signal. The frequency spectra for the mean intensities of sample 1 and sample 2 were plotted.

76

Chapter 6

Discussion

6.1 Numerical Results

To start with, the physics defining properties of the COMSOL model were examined. In total, a set of two different values were simulated for the absorption coefficient and thickness of the PDMS layer as well as the laser beam width. The resulting acoustic pressure proved that the model behaved as expected according to the physics; the acoustic pressure increased when the absorption coefficient, thickness and beam width were increased. For each parameter, the 2nd value were double the 1st value. Thus, it was possible to compare what value the model was most sensitive to changes in. By examining the acoustic pressure plots in Figures 5.1, 5.2 and 5.3 it became obvious that doubling the laser beam width resulted in the largest increase in pressure. The peak pressure was approximately fourfold. Doubling the absorption coefficient resulted in an approximate doubling of the acoustic pressure, while a twice as thick PDMS layer produced a less than double increase in the acoustic pressure. Plotting the intensity and temperature profiles inside the PDMS layer for both widths of the laser beam in Figure 5.4, gave an idea of why doubling this value caused such a large increase in acoustic pressure. The width of the area experiencing a rise in intensity was approximately doubled, which in turn caused the area of temperature increase to do the same. Moreover, the increase in temperature was higher when the beam width was doubled. By equation 2.9 it is known that the pressure rise in a material is proportional to its local rise in temperature. Hence, a larger beam width causes a higher rise in pressure in the PDMS layer, which in turn emits US waves of higher acoustic pressure.

Next, the frequency distribution of the simulated acoustic signal received by the transducer was

analysed. Four different absorption coefficients were examined for four different thicknesses of PDMS. For each combination, the center frequency, FWHM and percent bandwidth were calculated. The trend was similar for all thicknesses; the percent bandwidth and FWHM were increased when the absorption coefficient was decreased, while the center frequency was decreased. The most interesting part of the result was that the total amount of increase/decrease were larger for thicker layers of PDMS. This means that thicker films are more sensitive to the value of the absorption coefficient, or in other words how much toner particles are included in the film. Thus, a thicker film will experience more unwanted properties due to in-homogeneous distribution of the toner particles. The unwanted properties present themselves as a non-uniform acoustic pressure. Thus, before fabricating a PAF a study should be conducted to decide which combination of film thickness and amount of toner particles gives a satisfactory absorption of light without causing the system to be over sensitive to e.g. an uneven film surface. After deciding which thickness of film would be optimal, the RPM of the spin coating should be optimized as well to reduce imperfections in the films surface. It should be noted that these results were obtained for simulated signals that only included the incident wave, and the frequency spectrum would appear differently for a signal including reflected waves from the polystyrene layer in the model.

6.2 Experimental Results

The acoustic signal received by the ultrasonic transducer featured an incident wave and waves reflected from the bottom of the petri dish. Since the boundary where the waves were reflected consisted of a polymer on one side and air on the other, the reflection of the US waves was strong. Approximately 88 % of the energy of the incident wave was reflected back to the transducer from the bottom of the petri dish. Between the water and the petri dish, it was estimated that just 7 % of the incident wave energy would be reflected back to the transducer. These results were used to explain why the reflected wave had higher intensity than the incident wave for sample 2. For sample 1, however, the reflected wave had lower intensity than the incident wave. To explain this, the tilt of the samples were calculated.

For the calculations of tilting of the samples, it was found that sample 1 had a displacement in the z-axis between area 1 and area 2 equal to 18.75 μm. For sample 2, the largest displacement was found between area 1 and area 4 and equaled 14.9 μm. It should be noted that some of this displacement could be due to imperfections in the PAF. Imperfections could be caused by air bubbles trapped between the coating and petri dish or clusters of toner particles, or just arbitrary irregularities in the surface after spin coating. In the nano profile in Figure 3.4 the largest imperfection of the surface had a height of approximately 5 μm, this value could be used as an estimate for the uncertainty

of the tilt. From the intensity profiles plotted in Figures 5.13 and 5.14 it was noted that the wave reflected off the bottom of the petri dish had lower intensity than the incident wave for sample 1, while it had higher intensity for sample 2. This could also suggest that the petri dish containing sample 1 was more tilted than sample 2, causing the wave to be reflected from the bottom of the petri dish at an angle. Consequently, less of the intensity from the reflected wave would reach the UT.

To investigate if doubling the amount of toner particles in the PAF caused higher intensity US waves to propagate, the mean intensities over two 40 by 40 pixel areas were calculated and plotted in Figure 5.15. The areas were chosen in sections that had an approximately uniform distribution of toner particles. A shift corresponding to a spatial displacement of 116.2 μm between the surfaces of the samples was visible in the plot. Since the PAFs were spin coated with equal RPMs they should, in theory, have equal thicknesses. This offset could be due to the acoustic focusing, where the transducer position was adjusted in steps of 0.5 mm vertically while looking for the maximum amplitude of the acoustic echo. However, assuming that the film surfaces of the samples were leveled in the z-direction, one step of displacement in the focus would add up to a 500 μm spatial shift between the signals. Thus, it was concluded that the displacement was caused by the samples tilting in different directions.

For the 2nd sample, the amount of toner particles in the film was doubled from 0.5 grams to 1 gram. In theory, more toner particles should increase the absorption coefficient of the PAF, and thus increase the intensity of the generated US wave. By plotting the mean intensity over two arbitrary areas, it was observed that the maximum intensity in this area for sample 1 was $0.0051 \cdot 10^{-3}$, while the area in sample 2 had a maximum intensity of $0.0056 \cdot 10^{-3}$. This equals an approximate intensity increase of 9 % with double the amount of toner particles. However, it is not safe to say if this intensity increase was due to the larger amount of toner particles or due to other factors in the system. Several areas of the samples should be investigated to conclude if this was a trend. Next, the standard deviations from the mean intensities were calculated. They equaled $0.0026 \cdot 10^{-3}$ for both the sample areas. This means that the distribution of areas with and without toner particles were equal for the chosen areas in the two samples.

To conclude if the increase in intensity was a consequence of the larger amount of toner particles, a systematic study of several PAFs with varying amounts of toner particles should be conducted. However, it was not known what ratio of toner particles to PDMS was achievable before fully saturating the solution with particles.

6.3 Comparison of Results

One of the goals of this thesis was to create a simulation able to act as an estimate for a real-life experimental setup. Hence, the signals obtained from the experiment were compared to the previously simulated signals in both the time and the frequency domain. In Figure 5.17 the mean intensities over a small area for both sample 1 and sample 2 were compared to an arbitrary simulated signal. The simulated signal was generated from a model with a PDMS thickness of 15 μm and an absorption coefficient of $1/30$ μm^{-1}, the laser beam width was set to 5 μm. The signals were normalized and shifted to match each other. The waveform of the simulated signal was very similar to the waveforms generated by the PAF in the experiment. Similarly to the waveform for sample 2, the simulated reflected wave had higher intensity than the simulated incident acoustic wave. The main difference occured in the peak-to-peak amplitude of the incident waves, where the simulated signal had a much smaller amplitude. There are many possible reasons for this. The thickness of the film and the absorption coefficient of the material in the film decides how much of the energy from the laser light is absorbed in the film, and thus the intensity of the generated US waves. In the model used to simulate this acoustic signal, the PDMS thickness was set to 15 μm. From the nano profile of the PAF, its thickness was estimated to 13 μm. This difference was not too large, but it could cause different results when combined with the absorption coefficients. The absorption coefficient of the mixture of PDMS and toner particles was not known, but the absorption coefficient for PDMS only was estimated from Figure 3.6 to be 1.5 cm^{-1} for a 532 nm wavelength. The toner particles would increase it by some amount. Thus, different film thickness and different absorption coefficient was one of the reasons for the deviation between the intensity profiles of the experimental and numerical data. Moreover, the material properties between the simulated PDMS layer and the fabricated PAF were different since the film included toner particles which were not taken into account in the model.

Furthermore, the specifications for the laser beam and the ultrasonic transducer were different in the experimental setup and the model. As concluded in Section 5.1.1, out of the layer thickness, absorption coefficient and laser beam width, the model was most sensitive to changes in the beam width of the laser. Deviations in these specifications not only gave rise to differences in the time domain, but also in the frequency domain as observed in Figure 5.20. An estimate for the ultrasonic transducer frequency for the model was found to be 16 MHz, while the PVDF transducer used in the experimental setup had a 50 MHz frequency. The frequency spectrum for the simulated signal had a peak frequency of 15 MHz, while the frequency spectra of the mean intensities for sample 1 and sample 2 were shifted to the right compared to this. For sample 1 the peak frequency was 22.1 MHz, and sample 2 had a peak frequency of 28.9 MHz. However, these values could be shifted upwards due to the large frequency of the UT. In reality, they *could* be closer to the peak frequency

obtained for the simulated signal.

6.4 Critique of the Implementation

For both the numerical and the experimental parts of this thesis, there were several aspects that could have been improved:

- The dimensions of the PDMS layer in the model used for simulations deviated from the thicknesses measured for the fabricated PAFs. The analysis of the frequency distribution in the simulation was completed for PDMS thicknesses ranging from 15 μm to 45 μm, while the thickness of the PAFs was measured to approximately 13 μm. The reason for this was that the frequency distribution analysis was carried out before making the PAFs.

- The specifications for the laser and the ultrasonic transducer in the simulation were not in compliance with the specifications of the components included in the experimental setup. Again, the reason for this was that the experimental investigations were carried out after the numerical results were obtained. However, overall there should have been a greater similarity between the properties defined in the simulation and the properties of the real-life setup. This would have increased the quality of the results obtained from comparison between the simulated and experimental results as well.

- Due to time restrictions, the photoacoustic imaging were only completed for two PAFs with different amount of black toner particles. A natural extension of this work would be to fabricate several PAFs with different thicknesses and different amounts of toner particles, in order to make a better estimate for the achievable signal strength of this method.

- For the imaging optimization, the methods for focusing the ultrasonic transducer and for aligning the transducer with the laser beam could have been further developed. Optimizing these methods would also increase the received intensity from the acoustic wave. The transducer could have been displaced in smaller steps when it was close to the maximum amplitude, for a more precise focusing.

- More precision could have been used while leveling the samples to reduce the amount of tilting, which in turn could increase the accuracy of the received acoustic signals.

- In hindsight, the air bubbles included in the photoacoustic images for referencing had no immediate function for the results. It would have been preferable to do the scans over approximately homogeneous areas. That way, the calculations in this thesis could have been

carried out for the whole photoacoustic image instead. This would cause results of higher accuracy.

Chapter 7

Conclusion

7.1   Concluding Remarks

In this thesis, we have proposed a method for fabricating a PAF of a composite of black toner particles and PDMS. Two samples of a PAF with different amounts of toner particles have been examined. Sample 1 was made with 0.5 grams of toner particles, while sample 2 had 1 gram of toner particles to the same amount of PDMS solution. The intensity of the generated acoustic waves experienced an increase of approximately 9 % when the amount of toner particles was doubled. Thus, the experimental results indicated that toner particle based PAFs could be an option to increase the light absorption in BPAM. However, the extent of the experiments is not sufficient to claim that such PAFs are better than other alternatives. The method used to fabricate the PAFs can easily be repeated. Thus, an in-depth study with the goal of optimizing the thickness of the PAF and the amount of toner particles in the coating could be extended from the work done in this thesis.

In addition, we proposed a way to simulate the photoacoustic imaging system in COMSOL Multiphysics. The PAF was simulated as a thin layer of PDMS with an adjustable absorption coefficient, which could be changed to mimic adding or removing an amount of toner particles. An analysis regarding the frequency response of the acoustic signal simulated in the model was conducted. We concluded that both the absorption coefficient and the film thickness impacted the frequency response of the incident acoustic wave. However, for a thicker PDMS layer the frequency response was more sensitive to changes in the absorption coefficient. Thus, a thicker film would be subject to more unwanted properties arising from an in-homogeneous distribution of toner particles inside

the film. Overall, the resulting simulated acoustic signals were promising in the sense that they were similar to the real-life acoustic signals obtained from the experiments.

However, the simulation lacked accuracy in the specifications used to define the properties of the laser light and the ultrasonic transducer, compared to the components employed in the experimental setup. The reason for this was that the numerical calculations were carried out before the experiment, and thus these specifications were unknown at the time. Due to time restrictions the simulation was not completed with a set of more accurate values. The model parameters can of course be customized to simulate other setups for further research.

7.2 Further Outlook

As a continuation of the work presented in this thesis, it would be very interesting to investigate the following topics:

- **Soot particle based PAFs:** For future research studies it is suggested to look at other production methods of PAFs. One method that seems attractive for producing nano-pigments, is the use of soot from combustion flames. For example in [33], where composites from PDMS and soot produced from candle lights have been explored, and achieved signal strengths two order of magnitudes higher than previously reported. In [34], soot internally mixed with sulfuric acid resulted in a significant enhancement of both light absorption and scattering.

- **Phase imaging based in BPAM:** For this approach it is suggested to use an experimental setup as shown in Figure 7.1. For this setup that can be realized using an inverted microscope, a PAF is placed directly underneath a sliced tissue sample. Point-like waves are excited locally inside the PAF using a focused laser, and then picked-up by an ultrasonic transducer on the opposite side. For a combination of thin samples and transducers with a large f-number as illustrated in Figure 7.1 (a), the phase reconstruction can be simplified by assuming the sample to be a monolayer with respect to the expected axial resolution. The use of a a transducer with a large f-number will simplify the reconstruction further, by assuming that only waves transmitted normal to the monolayer will be received by the transducer. This yields a local approach where the measured wave delay only depends on a single pixel as shown in Figure 7.1 (a). The accuracy of this simple model, can probably be enhanced significantly by using a more sophisticated global approach as illustrated in Figure 7.1 (b). Here the sample is assumed to contain several pixel layers, and the full aperture opening of the transducer is included. In order to estimate the phase velocity in such a case, information from a number

of neighbor measurement positions have to be combined in order to reconstruct the sample volume.
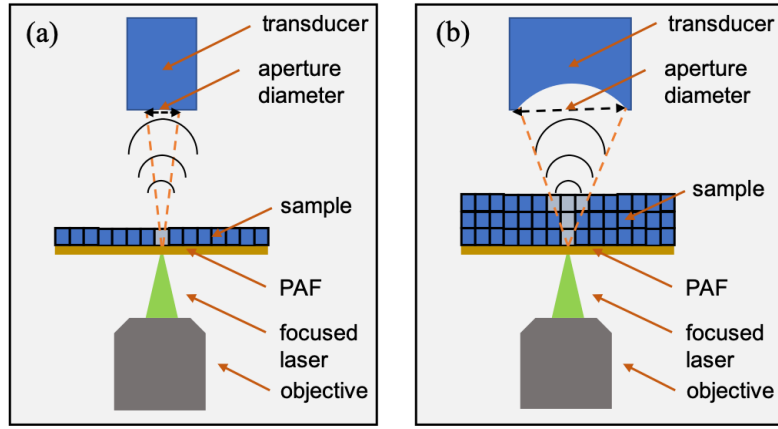

Figure 7.1: A proposed experimental setup for BPAM. A PAF is placed directly under the object to be imaged, and a pulsed laser is focused inside the film to generate acoustic waves.

Bibliography

[1] Ziskin MC, MD, MS. Fundamental Physics of Ultrasound and Its Propagation in Tissue [Journal Article]. RadioGraphics. 1993;13:705–709.

[2] Valluru KS, Willmann JK. Clinical photoacoustic imaging of cancer [Journal Article]. Ultrasonography. 2016;35:267–280.

[3] Manohar S, Razansky D. Photoacoustics: a historical review [Journal Article]. Advances in Optics and Photonics. 2016;8(4):586–617.

[4] Zhou Y, Yao J, Wang LV. Tutorial on photoacoustic tomography [Journal Article]. Journal of Biomedical Optics. 2016;21(6).

[5] Shimadzu. Near-Infrared Region Measurement and Related Considerations Part 1 [Web Page]. Shimadzu Corporation;. Available from: `https://www.shimadzu.com/an/ftir/support/tips/letter9/nir1.html`.

[6] Radio2space. Components of electromagnetic spectrum [Web Page]. PrimaLuceLab; 2013. Available from: `https://www.radio2space.com/components-of-electromagnetic-spectrum/`.

[7] Brunker J, Yao J, Laufer J, Bohndiek SE. Photoacoustic imaging using genetically encoded reportes: a review [Journal Article]. Journal of Biomedical Optics. 2017;22(7).

[8] Beard P. Biomedical photoacoustic imaging [Journal Article]. Interface Focus. 2011;1:602–631.

[9] Strohm EM, Moore MJ, Kolios MC. Single Cell Photoacoustic Microscopy: A review [Journal Article]. IEEE Journal of selected topics in quantum electronics. 2016;22(3).

[10] Elert G. The Physics Hypertextbook [Electronic Book Section]; 1998-2020. Available from: `https://physics.info/elasticity/`.

[11] Chestnutt B. Elasticity of Materials: Moduli & Measurements [Web Page]; 2016. Available from: `https://study.com/academy/lesson/elasticity-of-materials-moduli-measurements.html`.

[12] NDT Resource Center. Modes of Sound Wave Propagation [Web Page]; 2001-. Available from: `https://www.nde-ed.org/EducationResources/CommunityCollege/Ultrasonics/Physics/modepropagation.htm`.

[13] Garrido JA. Rayleigh Surface Acoustic Wave (SAW) devices [Web Page]. Technical University of Munich;. Available from: `http://w3.ualg.pt/~hgomes/html/classes/Biosensores/piezo/saw1.pdf`.

[14] Paschotta R. Bandwidth [Web Page]. RP-Photonics;. Available from: `https://www.rp-photonics.com/bandwidth.html`.

[15] Edmund Optics. Understanding Spatial Filters [Web Page]. Edmund Optics Inc.; 2020. Available from: `https://www.edmundoptics.com/knowledge-center/application-notes/lasers/understanding-spatial-filters/`.

[16] Thorlabs Inc . Principles of Spatial Filters [Web Page]. Thorlabs, Inc.; 1999-2020. Available from: `https://www.thorlabs.com/newgrouppage9.cfm?objectgroup_id=10768`.

[17] NDT Resource Center. Reflection and Transmission Coefficients (Pressure) [Web Page]; 2001. Available from: `https://www.nde-ed.org/EducationResources/CommunityCollege/Ultrasonics/Physics/reflectiontransmission.htm`.

[18] WARWICK. Heat Diffusion Equation [Web Page]. WARWICK; 2010. Available from: `https://warwick.ac.uk/fac/sci/physics/intranet/pendulum/heatdiffusion/`.

[19] MERCK. PDMS based polymer [Web Page]. Sigma-Aldrich; 2020. Available from: `https://www.sigmaaldrich.com/materials-science/material-science-products.html?TablePage=113790985`.

[20] Rahman MFA, Arshad MR, Manaf AA, Yaacob MIH. An investigation on the behaviour of PDMS as a membrane material for underwater acoustic sensing [Journal Article]. Indian Journal of Geo-Marine Sciences. 2012;41(6):557–562.

[21] Brahme A. 10.08.3. In: Ultrasound Interaction with Tissue. Elsevier; 2014. .

[22] Engineering ToolBox. Velocity of Sound in Solids and Metals [Web Page]; 2004. Available from: `https://www.engineeringtoolbox.com/sound-speed-solids-d_713.html`.

[23] Lochab J, Singh VR. Acoustic behaviour pf plastics for medical applications [Journal Article]. Indian Journal of Pure and Applied Physics. 2004;42:595–599.

[24] Habib A. PDMS preparation protocol [Manuscript];.

[25] Vlachos K. Absorption coefficient of Poly-dimethyl-siloxane (PDMS) material [Figure]; 2012. Available from: `https://www.researchgate.net/publication/235444247_Guiding_and_thermal_properties_of_a_hybrid_polymer-infused_photonic_crystal_fiber/figures?lo=1`.

[26] Smith SW. 7. In: Properties of Convolution; Correlation. California Technical Publishing; 2001. .

[27] Frei W. Modeling Laser-Material interactions with the Beer-Lambert Law [Web Page]. COMSOL Blog; 2015. Available from: `https://www.comsol.com/blogs/modeling-laser-material-interactions-with-the-beer-lambert-law/`.

[28] Müller A, Wapler MC, Wallrabe U. A quick and accurate method to determine the Poisson's ratio and the coefficient of thermal expansion of PDMS [Journal Article]. Soft Matter. 2019;(4):779–784.

[29] Ma J, Zhao M, Huang X, Bae H, Chen Y, Yu M. Low cost, high performance white-light fiber-optic hydrophone system with a trackable working point [Journal Article]. Optics Express. 2016;24(17).

[30] Bower AF. 3. In: Constitutive Models - Relations between Stress and Strain; 2008. .

[31] NDT Resource Center. Radiated Fields of Ultrasonic Transducers [Web Page]; 2001. Available from: `https://www.nde-ed.org/EducationResources/CommunityCollege/Ultrasonics/EquipmentTrans/radiatedfields.htm`.

[32] NDT Resource Center. Ultrasonic inspection - Near Field Calculation [Web Page]. NDT Resource Center; 2001. Available from: `https://www.nde-ed.org/GeneralResources/Formula/UTFormula/near_field/near.htm`.

[33] Wei-Yi Chang et al . Evaluation of Photoacoustic Transduction Efficiency of Candle Soot Nanocomposite Transmitters [Journal Article]. IEEE Transactions on Nanotechnology. 2018;17(5):985–993.

[34] Khalizov AF, Xue H, Wang L, Zheng J, Zhang R. Enhanced Light Absorption and Scattering by Carbon Soot Aerosol Internally Mixed With Sulfuric Acid [Journal Article]. J Phys Chem A. 2009;113(6):1066–1074.

Appendix A

Ibidi Petri Dish

Instructions
μ–Dish 50mm, low

μ–Dish 50mm, low Family

The μ–Dish 50mm, low is available with the ibiTreat surface and uncoated.

μ–Dish 50mm, low

Cat. No.	Description	Characteristics
81136	μ–Dish 50mm, low ibiTreat: ⌀ 50 mm, low wall (3 ml volume), #1.5 polymer coverslip, tissue culture treated	hydrophilic, sterilized
81131	μ–Dish 50mm, low Uncoated: ⌀ 50 mm, low wall (3 ml volume), #1.5 polymer coverslip	hydrophobic, sterilized

μ–Dish 35mm, low

Cat. No.	Description	Characteristics
80136	μ–Dish 35mm, low ibiTreat: ⌀ 35 mm, low wall (800 μl volume), #1.5 polymer coverslip, tissue culture treated	hydrophilic, sterilized
80131	μ–Dish 35mm, low Uncoated: ⌀ 35 mm, low wall (800 μl volume), #1.5 polymer coverslip	hydrophobic, sterilized

μ–Dish 35mm, high

Cat. No.	Description	Characteristics
81156	μ–Dish 35mm, high ibiTreat: ⌀ 35 mm, high wall (2 ml volume), #1.5 polymer coverslip, tissue culture treated	hydrophilic, sterilized
81151	μ–Dish 35mm, high Uncoated: ⌀ 35 mm, high wall (2 ml volume), #1.5 polymer coverslip	hydrophobic, sterilized

For research use only!

Instructions
μ–Dish 50mm, low

The Ibidi product family is comprised of a variety of μ–Slides and μ–Dishes, which have all been designed for high–end microscopic analysis of fixed or living cells. The high optical quality of the material is similar to that of glass, so you can perform all kinds of fluorescence experiments with uncompromised resolution and choice of wavelength.

The μ–Dish 50mm, low allows you to perform high resolution microscopy in a 50 mm Petri-dish with 9 mm walls. The low height makes high numerical apertures of Köhler illumination possible and provides large access for micromanipulation. The lid can be closed to hinder evaporation during long term experiments.

Shipping and Storage

The μ–Slides, μ–Dishes and μ–Plates are sterilized and welded in a gas-permeable packaging. The shelf life under proper storage conditions (in a dry place, no direct sunlight) is listed in the following table.

Conditions	
Shipping conditions	Ambient
Storage conditions	RT (15–25°C)

Surface and Coating

The μ–Dish is available with ibiTreat and uncoated surface. The ibiTreat surface is a physical treatment and optimized for adhesion of most cell types. Many cell lines as well as primary cells were tested for good cell growth. Uncoated as a very hydrophobic surface and allows no direct cell growth. It is suitable for specific coatings or suspension cells.

The uncoated μ–Dish must be coated to promote cell adhesion. If you like to establish a particular coating for your demands we recommend to test your coating procedure on uncoated and ibiTreat μ–Dishes, since we have observed that some biomolecules adhere differently to hydrophobic or hydrophilic plastic surfaces.

- Prepare your coating solution according to the manufacturer's specifications or reference. Prepare your μ–Dish, ibiTreat or uncoated. Adjust the concentration to a coating area of 7.9 cm² and 700 μl.

- Apply 700 μl into the growth area. Make sure that the entire bottom is covered with liquid easily tilting

Material

Ibidi μ–Slides, μ–Dishes and μ–Plates are made of a plastic that has the highest optical quality. The polymer coverslip on the bottom exhibits extremely low birefringence and autofluorescence, similar to that of glass. Also, it is not possible to detach the bottom from the upper part.

The μ–Slides, μ–Dishes and μ–Plates are not autoclavable, since they are only temperature-stable up to 80°C/175°F.

Please note that gas exchange between the medium and incubator's atmosphere occurs partially through the polymer coverslip, which should not be covered.

Optical Properties Ibidi Polymer Coverslip

Refractive index n_D (589 nm)	1.52
Abbe number	56
Thickness	No. 1.5 (180 μm)
Material	polymer coverslip

Shelf Life of Different Surfaces

ibiTreat, Glass Bottom, ESS	36 months
Collagen, Poly-L-Lysine	18 months

Please note! The Ibidi polymer coverslip is compatible with certain types of immersion oil only. A list of suitable oils can be found on page 3.

Geometry

Geometry of the μ–Dish 50mm, low

Diameter dish	50 mm
Volume	3 ml
Growth area	7.0 cm²
Diameter growth area	30 mm
Coating area using 700 μl	7.9 cm²
Height with / without lid	12 mm / 9 mm
Bottom matches coverslip	No. 1.5

Appendix B

PVDF Transducer

OLYMPUS

Tel: 781-419-3900
www.olympus-ims.com

TRANSDUCER DESCRIPTION

PART NO.: PI50-2-R0.50
SERIAL NO: 200637
DESIGNATION: .5 IN FOCUS OLF

FREQUENCY: 50.00 MHz
ELEMENT SIZE: .25 in. DIA.

TEST INSTRUMENTATION

PULSER/RECEIVER: PANAMETRICS 5601
DIGITAL OSCILLOSCOPE: LeCroy LC564A / SN: LC56410253
TEST PROGRAM: TP103-3
CABLE: RG 174/U LENGTH: 4FT

TEST CONDITIONS

PULSER SETTING: Energy: 1; Damping: 50 Ohm
RECEIVER SETTING: Gain: 46 dB; Attn: 52 dB
TARGET: .75/STEEL BALL/E
JOB CODE: TPP200

WATER PATH: 0.120 in

MEASUREMENTS PER ASTM E1065

FOCAL LENGTH — 0.495 in
WAVEFORM DURATION:
-14DB LEVEL — 0.044 US
-20DB LEVEL — 0.062 US
-40DB LEVEL — 0.107 US

SPECTRUM MEASURANDS:
CENTER FREQ. — 38.15 MHz
PEAK FREQENCY — 35.40 MHz
-6DB BANDWIDTH — 71.92 %
F#: 39.9

COMMENTS:

.75in STEEL BALL AS EQUAL PHASE REFLECTOR

** ACCEPTED, AUTH. BY: DATE: 02-25-2017

TECHNICIAN (7)   DATE: 02-25-2017

SIGNAL WAVEFORM

(0.05 USEC / DIVISON)

(VOLT)

FREQUENCY SPECTRUM

24.43   51.87

(MHz)
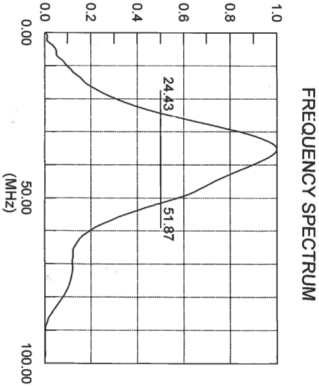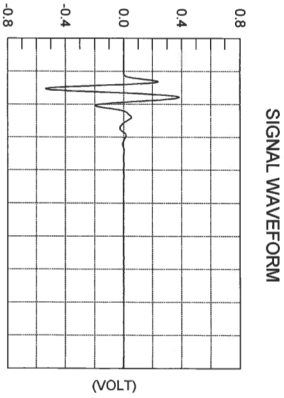
TP103 Rev. A

Appendix C

Laser Specifications

The laser used in the experimental setup is indicated by the red square.

Elforlight SPOT lasers produce pulse widths of < 2ns at repetition rates from single shot up to >50 kHz.

The short pulses are created by a combination of short cavity lengths and a novel fast electro-optic q-switching technique.

Applications include laser induced fluorescence, time resolved fluorescence, micromachining, biotechnology, plasma generation, remote sensing, photo acoustic imaging, MALDI mass spectrometry and MALDI imaging.

Model Name	SPOT-10-500-1064	SPOT-10-100-532	SPOT-10-200-532	SPOT-10-100-355
Wavelength	1064nm	532nm	532nm	355nm
Maximum Pulse Energy @ ≤ 10kHz	50µJ	10µJ	20µJ	10µJ
Minimum Pulse Width	< 2ns	< 1.8ns	< 1.8ns	<1.5ns
Repetition Rate	Single shot to > 50kHz			
Jitter	< +/- 1ns from external trigger input (typ.0.5ns)			
Power Stability	<+/- 2 % over 8 hours			
Spatial Mode	TEM$_{00}$, M^2 < 1.2			
Beam Diameter	~ 1mm			
Operating temp.	10-35 deg. C			
Laser Head Size	220mm long x 122mm x 60mm			
Controller Size	350mmx 260mm x 120mm			
Frequency Control	TTL trigger input required at up to 50kHz			
Cooling	Air cooled			
Power requirement	100 - 240 VAC, 50 / 60 Hz Max 100W			